ISTANBUL TECHNICAL UNIVERSITY ★ GRADUATE SCHOOL

ELECTROMAGNETIC SCATTERING BY TWO DIMENSIONAL CIRCULAR CYLINDERS WITH APERTURES

Ph.D. THESIS

Ömer Faruk ALPEREN

Department of Applied Informatics

Information and Communication Engineering Programme

JANUARY 2026

ISTANBUL TECHNICAL UNIVERSITY ★ GRADUATE SCHOOL

ELECTROMAGNETIC SCATTERING BY TWO DIMENSIONAL CIRCULAR CYLINDERS WITH APERTURES

Ph.D. THESIS

Ömer Faruk ALPEREN
(708202001)

Department of Applied Informatics

Information and Communication Engineering Programme

Thesis Advisor: Prof. Dr. Vasil TABATADZE
Thesis Co-Advisor: Assoc. Prof. Dr. Kamil KARAÇUHA

JANUARY 2026

ISTANBUL TEKNİK ÜNİVERSİTESİ ★ LİSANSÜSTÜ EĞİTİM ENSTİTÜSÜ

AÇIKLIKLARI OLAN İKİ BOYUTLU DAİRESEL SİLİNDİRLERDEN ELEKTROMANYETİK SAÇILMA

DOKTORA TEZİ

Ömer Faruk ALPEREN
(708202001)

Bilişim Uygulamaları Anabilim Dalı

Bilgi ve Haberleşme Mühendisliği Programı

Tez Danışmanı: Prof. Dr. Vasil TABATADZE
Eş Danışman: Doç. Dr. Kamil KARAÇUHA

OCAK 2026

Ömer Faruk ALPEREN is İTU Informatics Enstitute Ph.D student ID 708202001, successfully defended the thesis entitled "ELECTROMAGNETIC SCATTERING BY TWO DIMENSIONAL CIRCULAR CYLINDERS WITH APERTURES", which he prepared accordance with the requirements in the associated legislations, before giving the jury listed below.

Thesis Advisor :	**Prof. Dr. Vasil TABATADZE** İstanbul Technical University	.....
Co-advisor :	**Assoc.Prof.Dr. Kamil KARAÇUHA** İstanbul Technical University	.....
Jury Members :	**Asst. Prof. Dr. Sebahattin EKER** Istanbul Technical University	.....
	Prof. Dr. Hülya SERAB Yıldız Technical University	.....
	Assoc. Prof. Dr. Fatih DİKMEN Gebze Technical University	.....
	Asst. Prof. Dr. Cemanur AYDINALP PENÇE İstanbul Technical University	.....
	Prof. Dr. Selçuk PAKER İstanbul Nişantaşı University	.....

Date of Submission : 29 December 2025
Date of Defense : 28 January 2026

To my family,

FOREWORD

I would like to thank my advisor Prof. Dr. Vasil TABATADZE and my co-advisor Assoc. Prof. Dr. Kamil KARAÇUHA for their guidance and support as my advisors. Their unwavering support, encouragement, and belief in my abilities have been the foundation upon which this work has been built. Without their understanding, this thesis would not have been possible. It is with great pleasure and pride that I present this work, knowing that it has been shaped by the contributions of those who have walked this path with me.

January 2026 Ömer Faruk ALPEREN

TABLE OF CONTENTS

Page

FOREWORD ..... **ix**
TABLE OF CONTENTS ..... **xi**
ABBREVIATIONS ..... **xiii**
SYMBOLS ..... **xv**
LIST OF FIGURES ..... **xvii**
SUMMARY ..... **xix**
ÖZET ..... **xxi**
1. INTRODUCTION **1**
1.1 Motivation of Thesis 3
1.2 Literature Review 5
1.3 Contribution of the Thesis 7
2. ELECTROMAGNETIC SCATTERING H-POLARIZED LINE SOURCE BY A DOUBLE-SIDED IMPEDANCE CIRCULAR STRIP **11**
2.1 Formulation of The Problem 11
2.2 Numerical Results and the Comparison 23
2.2.1 Numerical results 24
2.2.2 Comparison and convergence 30
2.3 Outcomes 35
3. ELECTROMAGNETIC LINE SOURCE SCATTERING BY THE CIRCULAR ARC WITH FRACTIONAL BOUNDARY CONDITION **37**
3.1 The Formulation of The Problem 37
3.2 Numerical Results and the Comparison 44
3.3 Outcomes 58
4. CONCLUSION AND RECOMMENDATIONS **61**
REFERENCES **63**
CURRICULUM VITAE **69**

ABBREVIATIONS

FEM	**:** Finite Element Method
FTDT	**:** Finite Time Domian Technique
MAS	**:** Method of Auxiliary Source
MoM	**:** Method of Moments
PEC	**:** Perfect Electric Conductor
PMC	**:** Perfect Magnetic Conductor
PTD	**:** Physical Diffraction Theory
TE	**:** Transverse Electric
TRCS	**:** Total Radar Cross Section

SYMBOLS

$\boldsymbol{k}$	**:** Wavenumber ($k = \omega\sqrt{\mu\varepsilon}$)
$\boldsymbol{\omega}$	**:** Angular frequency
$\boldsymbol{\mu}$	**:** Permeability of medium
$\boldsymbol{\varepsilon}$	**:** Permittivity of medium
$\boldsymbol{Z}$	**:** Surface impedance
$\boldsymbol{\eta}$	**:** Intrinsic impedance of medium
$\boldsymbol{\alpha}$	**:** Fractional order of boundary condition
$\boldsymbol{H}$	**:** Magnetic field
$\boldsymbol{E}$	**:** Electric field
$\boldsymbol{a, b}$	**:** Inner and outer radii of circular arc
$\boldsymbol{\theta}$	**:** Angular coordinate
$\boldsymbol{r}$	**:** Raidal coordinate
$\boldsymbol{\rho}$	**:** Distance between source and observation point
$\boldsymbol{C_n^{(v)}(x)}$	**:** Gegenbauer polynomial
$\boldsymbol{J_m(x)}$	**:** Bessel function of the first kind
$\boldsymbol{H_m^{(1)}(x)}$	**:** Hankel function of the first kind
$\boldsymbol{\Gamma(x)}$	**:** Gamma function
$\boldsymbol{i}$	**:** Imaginary unit $i = (\sqrt{-1})$

LIST OF FIGURES

Page

Figure 2.1 : The geometry of the problem. **12**
Figure 2.2 : TRCS for the line source is located inside of different impedance values ranging from PEC to PMC in the limit cases ($\alpha = 1$)..... **24**
Figure 2.3 : TRCS for the line source is located outside for different impedance values ranging from PEC to PMC in the limit cases ($\alpha = 1$)..... **25**
Figure 2.4 : TRCS for the line source is located inside for different aperture sizes while other parameters are constant ($\alpha = 1$). **26**
Figure 2.5 : TRCS for the line source and its located inside ($\alpha = 1$)..... **27**
Figure 2.6 : Near H-field amplitudes for different parameters when the source is located inside ($\theta = \pi - \frac{\pi}{3}, a = 1$). **28**
Figure 2.7 : Near H- field amplitudes for different positions of the line source ($\theta = \pi - \frac{\pi}{3}, a = 1, k = 3.38$). **29**
Figure 2.8 : TRCS comparison with PEC circular strip for ($\theta = \pi - \frac{\pi}{4}, a = 1$)..... **30**
Figure 2.9 : The normalized near H-field comparison with the different source excitations for ($\theta = \pi - \frac{\pi}{4}, k = 2.3, a = 1$)..... **31**
Figure 2.10 : The normalized near H-field comparison for PEC and Impedance Surface ($\theta = \pi - \frac{\pi}{4}, k = 2.3, a = 1$) … **32**
Figure 2.11 : Convergence of the boundary conditions for ($\theta_0 = \pi - \frac{\pi}{3}, a = 1$). ... **33**
Figure 2.12 : The comparison of the total field H_z distributions with (a) Orthogonal Polynomials Method for perfect electric conducting (PEC) surface [25], (b) embedding formulae method [55], and the proposed method with ($\xi_1 = \xi_2 = 0.001$). **34**
Figure 2.13 : The resonance characteristics for small apertures $\theta = \pi - \pi/100$ and $\theta_0 = \pi$..... **35**
Figure 3.1 : The geometry of the problem-2. ..... **38**
Figure 3.2 : Source location is $x = 0.7,\ y = 0$ and aperture size is $\theta = \pi - \frac{\pi}{3}$, observation points $\alpha = 0.0001,\ 0.25,\ 0.5,\ 0.75,\ 1$ **45**
Figure 3.3 : Source location is $x = -0.7,\ y = 0$ and aperture size is $\theta = \pi - \frac{\pi}{3}$, observation points $\alpha = 0.0001,\ 0.25,\ 0.5,\ 0.75,\ 1$ **46**
Figure 3.4 : Source location is $x = 0,\ y = 0.7$ and aperture size is $\theta = \pi - \frac{\pi}{3}$, observation points $\alpha = 0.0001,\ 0.25,\ 0.5,\ 0.75,\ 1$ **46**
Figure 3.5 : Source location is $x = 0,\ y = -0.7$ and aperture size is $\theta = \pi - \frac{\pi}{3}$, observation points $\alpha = 0.0001,\ 0.25,\ 0.5,\ 0.75,\ 1$ **47**
Figure 3.6 : Source location is $x = -1.5,\ y = 0$ and aperture size is $\theta = \pi - \frac{\pi}{3}$, observation points $\alpha = 0.0001,\ 0.25,\ 0.5,\ 0.75,\ 1$ **47**
Figure 3.7 : Source location is $x = -1.5,\ y = -1.3$ and aperture size is $\theta = \pi - \frac{\pi}{3}$, observation points $\alpha = 0.0001,\ 0.25,\ 0.5,\ 0.75,1$ **48**

Figure 3.8 : Source location is $x = -1.7,\ y = 0$ and aperture size is $\theta = \pi - \frac{\pi}{3}$, observation points $\alpha = 0.0001,\ 0.25,\ 0.5,\ 0.75,\ 1$ **48**
Figure 3.9 : Source location is $x = -1.7,\ y = -1.5$ and aperture size is $\theta = \pi - \frac{\pi}{3}$, observation points $\alpha = 0.0001,\ 0.25,\ 0.5,\ 0.75,\ 1$ **49**
Figure 3.10 : Source location is $x = -1.7,\ y = -1.7$ and aperture size is $\theta = \pi - \frac{\pi}{3}$, observation points $\alpha = 0.0001,\ 0.25,\ 0.5,\ 0.75,\ 1$ **49**
Figure 3.11 : Source location is $x = -1.8,\ y = 0$ and aperture size is $\theta = \pi - \frac{\pi}{3}$, observation points $\alpha = 0.0001,\ 0.25,\ 0.5,\ 0.75,\ 1$ **50**
Figure 3.12 : Source location is $x = -1.8,\ y = -1.5$ and aperture size is $\theta = \pi - \frac{\pi}{3}$, observation points $\alpha = 0.0001,\ 0.25,\ 0.5,\ 0.75,\ 1$ **50**
Figure 3.13 : Source location is $x = -1.8,\ y = -1.7$ and aperture size is $\theta = \pi - \frac{\pi}{3}$, observation points $\alpha = 0.0001,\ 0.25,\ 0.5,\ 0.75,\ 1$ **51**
Figure 3.14 : Source location is $x = -0.7,\ y = 0$ and different aperture sizes $\theta = \pi - \pi/5\,, \pi - \pi/4\,, \pi - \pi/3\,, \pi - \pi/2\,, \pi - 2\pi/3.$ **51**
Figure 3.15 : Source location is $x = -1.5,\ y = -1.3$ and different aperture sizes $\theta = \pi - \pi/5\,, \pi - \pi/4\,, \pi - \pi/3\,, \pi - \pi/2\,, \pi - 2\pi/3$..... **52**
Figure 3.16 : Source location is $x = -1.7,\ y = -1.5$ and different aperture sizes $\theta = \pi - \pi/5\,, \pi - \pi/4\,, \pi - \pi/3\,, \pi - \pi/2\,, \pi - 2\pi/3$..... **53**
Figure 3.17 : Source location is $x = -1.7,\ y = -1.7$ and different aperture sizes $\theta = \pi - \pi/5\,, \pi - \pi/4\,, \pi - \pi/3\,, \pi - \pi/2\,, \pi - 2\pi/3$..... **54**
Figure 3.18 : Source location is $x = -1.8,\ y = -1.5$ and different aperture sizes $\theta = \pi - \pi/5\,, \pi - \pi/4\,, \pi - \pi/3\,, \pi - \pi/2\,, \pi - 2\pi/3$..... **55**
Figure 3.19 : Source location is $x = -1.8,\ y = -1.7$ and different aperture sizes $\theta = \pi - \pi/5\,, \pi - \pi/4\,, \pi - \pi/3\,, \pi - \pi/2\,, \pi - 2\pi/3$..... **56**
Figure 3.20 : Source location is $x = -0.7,\ y = 0$, for (b) constant is $kk = 1{,}57962.$ and aperture size is $\theta = \pi - \pi/5$, for (c) constant is kk =2,96677 and aperture size is $\theta = \pi - \pi/5$ **57**
Figure 3.21 : Source location is $x = -0.7,\ y = 0$, for (b) constant is $kk = 1{,}15423.$ and aperture size is $\theta = \pi - \pi/5$, for (c) constant is kk =2,48589 and aperture size is $\theta = \pi - \pi/5$ **58**

ELECTROMAGNETIC SCATTERING BY TWO DIMENSIONAL CIRCULAR CYLINDERS WITH APERTURE

SUMMARY

In this thesis, investigated the scattering of an H-polarized electromagnetic line source from circular strip structures within an analytical-numerical framework. The first stage of the study considers circular strip geometries with classical impedance boundary conditions; this formulation is then generalized using fractional boundary conditions. The aim is to define a continuous transition between ideal boundary behavior and impedance-controlled surfaces.

The theoretical formulation is developed in a cylindrical coordinate system, and the incident and scattered magnetic fields are explicitly expressed. The induced current densities on the scattering surface are represented using orthogonal polynomial expansions, primarily Chebyshev and Gegenbauer polynomials. This approach allows for the accurate fulfillment of the edge conditions required by the circular geometry, while also offering high numerical stability and fast convergence. Fractional boundary conditions are applied through a generalized Leontovich relation where the fractional order parameter determines the relationship between the tangential electric and magnetic field components. Because of this, we can correctly model the surface behaviours whih cannot be efficiently described like a classical integer order models.

Numerical analyses were performed to investigate the effects of parameters such as fractional order, surface impedance, aperture size, and the location of the line source on the scattering response. Evaluations were made considering the total radar cross section (TRCS) and near-field distributions. The results show that the resonance behavior is depend on the fractional order and the difference between the internal and external surface impedances. As the fractional order increases, shifts occur in the resonance characteristics, and significant changes are observed in the field's localization behavior. These effects do not appear in the results obtained with classical perfect electrical or magnetic conduction boundary conditions.

The accuracy and reliability of the proposed method were verified through comparisons with analytical results in the literature for limit cases representing ideal boundary conditions. The observed agreement and limited numerical deviations demonstrate the effectiveness of the orthogonal polynomial-based fractional formulation in terms of convergence and accuracy. Consequently, the analytical-numerical approach developed in this study offers a flexible and physically meaningful tool for investigating electromagnetic scattering from circular ribbon structures; it also provides a solid foundation for the analysis and design of resonance-controlled and impedance-based electromagnetic structures.

AÇIKLIĞI OLAN İKİ BOYUTLU DAİRESEL SİLİNDİRLERDEN ELEKTROMANYETİK SAÇILMA

ÖZET

Bu doktora tezinde, H-polarizasyonlu bir elektromanyetik çizgi kaynağının dairesel şerit geometrilerinden saçılması analitik ve nümerik olarak incelenmiştir. İlk aşamada, çift yüzeyli empedans sınır koşullarına sahip dairesel bir şerit için saçılma problemi ele alınmış; ardından bu yaklaşım kesirli sınır koşulları kullanılarak genelleştirilmiştir. Çalışmanın temel amacı, klasik elektromanyetik saçılma problemlerinde kullanılan sınır koşullarını genelleştirerek, daha karmaşık ve gerçekçi yüzey davranışlarını temsil edebilecek bir model ortaya koymaktır. Bu amaç doğrultusunda, hem teorik hem de hesaplamalı açıdan güçlü bir çözüm yaklaşımı olan ortogonal polinom yöntemi fraksiyonel sınır koşullarıyla birleştirilmiş, böylece elektromanyetik alan denklemlerinin çözümünde yüksek doğruluk ve hızlı yakınsama özellikleri bir arada elde edilmiştir.

Elektromanyetik saçılma problemleri, dalga teorisinin temel konularından biri olmakla birlikte radar, anten tasarımı, optik sistemler, biyomedikal görüntüleme, malzeme karakterizasyonu ve elektromanyetik uyumluluk gibi birçok mühendislik alanında doğrudan uygulama alanları bulunmaktadır. Bu kapsamda, dairesel şerit geometrisi, hem matematiksel olarak tanımlanabilirliği hem de birçok fiziksel sistemin idealize edilmiş modeli olması açısından özel bir öneme sahiptir. Ancak klasik yöntemlerde, yüzeyin yalnızca mükemmel iletken (PEC) veya mükemmel manyetik iletken (PMC) kabul edilmesi, gerçek malzemelerin karmaşık davranışlarını yansıtmakta yetersiz kalmaktadır. Bu tezde geliştirilen fraksiyonel sınır koşulu yaklaşımı, yüzeyin elektriksel ve manyetik tepkisini bir ara bölgede tanımlayarak, bu eksikliği ortadan kaldırmaktadır.

Fraksiyonel sınır koşulu, klasik Leontovich empedans modeli esas alınarak genelleştirilmiştir. Bu modelde yüzey empedansı, fraksiyonel bir mertebe parametresi aracılığıyla ifade edilmiştir. Bu parametre, yüzeyin elektriksel ve manyetik alanlar arasındaki etkileşimini kısmi türev dereceleriyle tanımlayarak klasik sınır koşullarına bir süreklilik kazandırmaktadır. Fraksiyonel mertebe sıfıra yaklaştığında sistem, mükemmel elektrik iletken (PEC) sınır koşuluna; bire yaklaştığında ise mükemmel manyetik iletken (PMC) koşuluna yaklaşmaktadır. Böylece, bu iki uç durum arasında kalan tüm olasılıklar, tek bir model üzerinden sürekli biçimde temsil edilebilmektedir. Bu yaklaşım, özellikle karmaşık empedans özellikleri gösteren yüzeylerin veya metamaterial yapıların modellenmesinde güçlü bir teorik temel sunmaktadır.

Matematiksel modelleme aşamasında, gelen ve saçılan manyetik alanlar silindirik koordinat sisteminde tanımlanmış, indüklenen akım yoğunlukları ise Chebyshev ve Gegenbauer polinomları cinsinden ifade edilmiştir. Bu polinomların ortogonallik

özellikleri, kenar koşullarının tam olarak sağlanmasını mümkün kılmıştır. Ayrıca bu yaklaşım, çözümün hızlı yakınsamasını sağlayarak sayısal kararlılığı artırmıştır. Kenar bölgelerinde meydana gelen alan tekillikleri, polinomların ağırlık fonksiyonları yardımıyla doğru biçimde modellenmiştir. Böylece, çözümün hem matematiksel hem de fiziksel olarak tutarlı olması sağlanmıştır.

Analitik formülasyonun ardından, fraksiyonel sınır koşulu parametresi, iç ve dış yüzeylerde farklı empedans değerleri olacak şekilde uygulanmıştır. Böylece, çift yüzeyli saçıcıların karmaşık elektromanyetik davranışları analiz edilmiştir. Geliştirilen yöntem kapsamında, saçılan alanın ifadesi Green fonksiyonu kullanılarak integral biçiminde elde edilmiş, daha sonra Fourier katsayılarına ayrılarak sistem denklemleri çözümlenmiştir. Sonuç olarak, iç ve dış yüzeylerdeki akım yoğunluklarını tanımlayan katsayılar, kapalı forma yakın analitik ifadelerle hesaplanmıştır.

Tez kapsamında gerçekleştirilen nümerik analizler, farklı fraksiyonel mertebe değerleri, empedans kombinasyonları, açıklık genişlikleri ve kaynak konumları için gerçekleştirilmiştir. Analizler sonucunda elde edilen Toplam Radar Kesit Alanı (TRCS) ve yakın alan dağılımı verileri, sistemin rezonans davranışlarını ayrıntılı biçimde ortaya koymuştur. Bulgulara göre, fraksiyonel mertebenin artmasıyla birlikte rezonans frekanslarının daha yüksek değerlere kaydığı ve alan yoğunluğunun belirli bölgelerde sıkışarak lokalize olduğu gözlemlenmiştir. Bu durum, klasik sınır koşullarıyla tanımlanamayan yeni rezonans tiplerinin varlığını göstermektedir. Ayrıca, iç ve dış yüzeylerdeki empedans farkının artması, sistemin rezonans genliğini belirgin biçimde yükseltmiş ve alan konsantrasyonunu keskinleştirmiştir.

Kaynak konumunun etkileri de detaylı biçimde incelenmiştir. Kaynağın dairesel şerit içindeki konumu değiştirildiğinde, hem alanın genliği hem de rezonans tepe noktalarının dağılımı önemli ölçüde değişmiştir. Kaynak merkeze yakın konumlandığında alan dağılımı daha simetrik ve lokalize iken, kenara yakın konumlarda alan yayılımı daha geniş ve karmaşık bir hâl almıştır. Bu bulgular, dairesel rezonatörlerin tasarımında kaynak yerleşiminin elektromanyetik performans üzerinde belirleyici olduğunu göstermektedir.

Yapılan karşılaştırmalı analizlerde, geliştirilen yöntemin doğruluğu literatürdeki mevcut çalışmalarla sınanmıştır. Mükemmel iletken sınır koşulu (PEC) altında elde edilen TRCS değerleriyle yapılan karşılaştırmalarda sapma oranı %1'in altında, yakın alan dağılımlarında ise %4'ün altında kalmıştır. Bu sonuçlar, yöntemin hem yüksek doğruluğa hem de hızlı yakınsamaya sahip olduğunu kanıtlamaktadır. Ayrıca önerilen yaklaşımın, az sayıda terimle yüksek hassasiyet sağlaması hesaplama maliyetini azaltarak yöntemi mühendislik uygulamaları için son derece uygun hale getirmiştir.

Bu çalışmanın bilimsel katkısı, fraksiyonel sınır koşullarının dairesel geometrilerde analitik biçimde uygulanabilmesini sağlayan ilk kapsamlı model olmasıdır. Böylece, yalnızca klasik sınır koşullarıyla sınırlı kalan mevcut çözümlerden daha genel bir teorik çerçeve elde edilmiştir. Ortogonal polinom yönteminin bu şekilde genişletilmesi, gelecekte farklı geometrilere (örneğin eliptik, silindirik veya karmaşık yüzeylere) uygulanabilecek güçlü bir altyapı oluşturmuştur. Model, aynı zamanda üç boyutlu problemlere veya farklı polarizasyon türlerine de uyarlanabilir niteliktedir.

Uygulama açısından bakıldığında, bu tezde geliştirilen yaklaşım özellikle anten tasarımı, radar kesit alanı optimizasyonu, rezonans yapılarının incelenmesi ve metamaterial tabanlı elektromanyetik yüzeylerin modellenmesi gibi alanlarda doğrudan kullanılabilir. Fraksiyonel sınır koşulu modeli, dalga yayılımını kontrol etme, yüzey empedansını istenen biçimde ayarlama ve enerji yoğunluğunu belirli bölgelerde toplama gibi mühendislik problemlerinde önemli avantajlar sunmaktadır. Bu yönüyle, çalışma yalnızca teorik bir katkı değil, aynı zamanda pratik mühendislik çözümlerine dönüştürülebilecek bir yöntem önermektedir.

Sonuç olarak, bu tez fraksiyonel sınır koşullarına sahip dairesel şeritlerde elektromanyetik saçılmanın çözümü için güçlü, kararlı ve genellenebilir bir yöntem ortaya koymuştur. Ortogonal polinom yöntemi ile fraksiyonel sınır koşullarının birleştirilmesi, klasik sınır koşullarını aşan yeni bir analitik çerçeve sunmuş ve elektromanyetik teorinin gelişimine önemli bir katkı sağlamıştır. Elde edilen sonuçlar, hem teorik araştırmalara ışık tutmakta hem de anten, radar ve malzeme mühendisliği gibi alanlarda geleceğe yönelik yüksek hassasiyetli tasarımlar için güçlü bir temel oluşturmaktadır.

1. INTRODUCTION

Electromagnetic scattering describes the response of material structures to incident electromagnetic waves and underpins a broad range of measurement, sensing, and communication technologies. In fields such as radar systems, antenna design, inverse scattering problems and electromagnetic imaging, accurate modeling of wave-matter interaction plays a important role in system performance [1],[2]. Therefore, understanding the mechanisms of electromagnetic scattering is important for both theoretical electromagnetic studies and for engineering applications.

In scattering theory, canonical geometries are often preferred to allow for a clearer examination of the fundamental physical mechanisms. Geometries such as linear strips, circular arcs, and cylindrical structures can be considered analytically, while also reflecting the fundamental properties of curved and finite conducting surfaces encountered in practical applications [3],[4],[5][6]. Studies on such canonical models explain the role of edges and apertures on diffraction mechanisms and how resonant behavior arises in many cases.

Within this set of problems, strip and arc geometries excited by linear sources offer a particularly instructive structure. Even in two-dimensional approaches, the presence of finite apertures and edge singularities can lead to complex field distributions and pronounced resonant responses [2]. Such geometries naturally occur in many electromagnetic structures such as antenna apertures, resonance cavities are therefore constantly being studied.

In electromagnetic scattering problems, the selection of boundary conditions directly affects the field distributions and scattering characteristics. Classical boundary conditions, based on the assumptions of perfect electric conductor (PEC) and perfect magnetic conductor (PMC), although they show suitable references, generally cannot adequately represent the electromagnetic behavior of real materials. To overcome this situation, approximate boundary conditions have been developed that describe the relationship between the tangential electric and magnetic field components on the

surface [7]. These approaches allow for a more flexible and realistic modeling of the boundary behavior of electromagnetic fields.

Impedance boundary conditions offer a more general form of approximate boundary conditions by considering both resistive and reactive properties of the surface. Through a single boundary relation, it enables the efficient modeling of electromagnetic field–surface interaction in lossy or coated materials [8]. The use of these boundary conditions has more expanded the scope of scattering analyses, especially those performed in finite and curved geometries.

The addition of impedance boundary conditions to circular and cylindrical geometries has had a decisive effect on resonance properties and scattering characteristics. Studies show that changes in surface impedance can lead to significant differences in resonance frequencies, field localization and total radar cross-section (TRCS) [9]. Thanks to these features, impedance-based models are effectively used in both direct scattering problems and in inverse scattering and electromagnetic imaging applications [10],[11],[12].

The progress of diffraction theory has accelerated with the emergence of analytical approaches that directly connect with boundary conditions. In this regard, Physical Theory of Diffraction (PTD) has provided solutions with higher accuracy by relating the electromagnetic field behaviors occurring in edge regions to the relevant boundary conditions [13]. In addition to this approach, studies have also been carried out to define edge conditions more accurately from a mathematical point of view [14].

Moreover, spectral field methods and integral equation approaches have enabled the investigation of finite and curved structures, thus expanding the analytical scope of diffraction problems [15], [16]. These methods allow for the accurate calculation of electromagnetic field distributions, especially in geometrically complex structures.

When considering studies that aim to achieve better results than classical boundary conditions, there are studies in the literature that address electromagnetic boundary behaviors in more general forms. These studies enable the generalization of impedance based models and allow boundary behaviors to be expressed with different physical interpretations [17].

As a continuation of these approaches, the introduction of the stuation of fractional operators and fractional boundary conditions has brought a different perspective to

electromagnetic scattering problems. Fractional boundary conditions, which provide a continuous transition between classical impedance models and ideal boundary conditions, have enabled a more flexible representation of surface behaviors [18].

Fractional boundary conditions have been applied to cylindrical and circular strip geometries in order to obtain new results in terms of resonance behavior. Studies show that such boundary conditions can lead to significant changes in scattering characteristics when compared with classical boundary models. [19], [20].

Circular strip geometries excited by H-polarized line sources create an important model because they are both analytically verifiable and capable of creating physically good results. Such structures allow for the systematic investigation of the effects of curvature, aperture size, source location, and surface properties on electromagnetic scattering.

The analytical-numerical investigation of these geometries provides a strong way for transitioning from classical scattering models to more general boundary conditions, and forms the basis of the work carried out in the following chapters of this thesis.

1.1 Motivation of Thesis

When electromagnetic scattering problems are studied, especially when dealing with geometries with finite dimension and curved surfaces, they present some problems from both theoretical and applied electromagnetic perspectives. In such problems, the wave behavior depends not only on the geometric properties of the structure but also on the electromagnetic characteristics of the surface. Studies on cylindrical and circular structures, in particular, reveal good physical results in terms of significant resonance effects and field concentrations [21],[22],[23].

Many research on circular and cylindrical geometries has focused on ideal boundary conditions or classical impedance models. While these boundary conditions or impedance models contribute to understanding fundamental electromagnetic mechanisms, they do not always adequately represent the complex surface behaviors observed in real materials. This is particularly evident when the surface impedance varies across different regions of the structure, highlighting insufficient models based on uniform boundary conditions [24].

The aim of this thesis is to contribute to the consideration of electromagnetic scattering problems under more general and flexible boundary conditions. Therefore, in the first stage of the study, circular strip geometries were investigated using classical impedance boundary conditions and it was shown where the possibilities offered by the current approaches reach their limits. These investigations create an important reference point, especially in terms of resonance behavior and its effects on the total radar cross section (TRCS) [25].

This frame of reference provides a starting point for transitioning to more general boundary conditions in later chapters of this thesis. One of the main purpose of this thesis is the investigation of fractional boundary conditions, which define a continuous transition between ideal boundary conditions and impedance based approaches, and which go beyond classical impedance models. This approach allows for a more realistic modeling of surface behavior and provides a new perspective on electromagnetic scattering problems.

At the same time, the nature of the solution method used also plays a important role in the aim of this study. While only numerical methods require high computation times when dealing with finite and curved geometries, and only analytical approaches also face various limitations in terms of geometric structure and boundary conditions. The analytical-numeric approach used in this thesis, based on orthogonal polynomial method, combines the advantages of both methods, enabling the correct fulfillment of edge conditions and the precise determination of resonance behavior. At the same time, the processing time has been reduced to a certain extent [3],[4].

As a result, the aim of this thesis is to move beyond scattering analyses based on classical impedance models and to focus on more general boundary conditions, to develop more flexible electromagnetic models for finite and curved geometries, and to solve these models using an analytically-numerically stable method. The goal is for the obtained results to contribute to electromagnetic theory and to provide a reliable reference that can be used in the design and analysis of antenna, resonator, and scatterer structures.

1.2 Literature Review

In recent years, the use of fractional boundary conditions in electromagnetic scattering problems has increasing interest because it offers a generalized modeling that goes beyond classical impedance models and ideal boundary conditions. Such approaches allow for a more flexible representation of surface behavior, especially in finite and curved geometries [26]. Studies on slotted cylindrical structures show that fractional boundary conditions are not only a theoretical approach but also a directly applicable model.

For this reason, analytical-numerical approaches developed for concentric cylindrical structures with different slit positions and numbers reveal the sensitivity of scattering behavior to parameters in E- and H-polarization cases in detail [27].These studies show that fractional boundary conditions can create significant differences in resonance and field distributions compared to classical impedance-based models. Similarly, fundamental approaches with impedance boundary conditions developed for arbitrarily shaped two-dimensional scatterers have shown that such generalized boundary models can be successfully applied to more complex geometries [28].

The theoretical foundations of fractional boundary conditions are more clearly understood when considered together with the classical sources of electromagnetic propagation and scattering theory. Studies providing a comprehensive framework for wave propagation, diffraction, and resonance problems support the mathematical infrastructure on which the analytical-numerical methods used are based [29]. In this context, studies investigating slotted cylindrical structures with different internal and external surface impedances have clearly shown that it is necessary to go beyond the uniform surface assumption [30].

The behavior of electromagnetic fields in edge regions is one of the fundamental elements determining the accuracy of the solution, especially in finite and open structures. General investigations into the behavior of electromagnetic fields in edge regions highlight the need for mathematical consistency of boundary conditions [31]. These studies also provide a notional basis for interpreting the effects of impedance-based and fractional boundary conditions on edge effects.

The general theory of electromagnetic scattering and diffraction problems has been promoted by common studies that evaluate the strengths and weaknesses of analytical

and numerical approaches [32]. Special functions, series expansions and integral representations used in problems related to cylindrical geometries stand out as the desired mathematical tools in solving such problems [33],[34]. This mathematical method has played a direct role in the improvment of analytic-numerical methods based on orthogonal polynomials.

Research into generalizing edge conditions in geometries limited by material plates has revealed the need to go beyond classical boundary assumptions and has contributed to the development of more flexible boundary models [35]. In terms of application, artificial intelligence and optimization based approaches to targeted direction of electromagnetic fields have brought a new perspective to scattering analysis and field control problems [36].

Studies involving infinite axial slits in circular cylindrical structures are among the first problems to be addressed in the investigation of diffraction mechanisms for H-polarization [37]. These studies provide a main analysis of finite and multi slit structures. In addition, scattering analyses of two dimensional spaces with random shapes reveal how important it is to consider geometric complexity as well as boundary conditions [38].

The handling of fractional boundary conditions using the Wiener–Hopf technique for semi-infinite plates has shown that fractional models can be applied in a manner compatible with classical analytical tools [39]. Similarly, analyses performed for TEP(Transverse Electric Polarized) waves in cylindrical structures with circular slits have revealed the effects of fractional and impedance based approaches on scattering behavior in different polarization states [40].

Analytical studies on space and resonator problems in the time domain have shown that the behavior of the electromagnetic field should be evaluated not only in steady-state conditions but also in time varying response [41]. Research focusing on determining the eigen frequencies of open resonators has clearly shown that geometric parameters play a important role in shaping the resonance characteristics [42]. In addition, studies aimed at increasing the quality factor in open two dimensional resonators have also revealed how the resonance behavior can be controlled from an engineering perspective [43].

Cylindrical and resonator structures containing advanced materials such as graphene have provided tunability to electromagnetic scattering and resonance problems. Graphene-coated Helmholtz resonators and similar structures demonstrate that scattering characteristics can be effectively controlled by material properties [44]. Studies in which fractional boundary conditions are addressed in strip geometries using Wiener–Hopf analysis have also made significant contributions to strengthening the mathematical consistency of the fractional model [45].

Analysis of induced surface currents in curved strips directly shows how electromagnetic fields are shaped by edge and curvature effects [46]. Electromagnetic models developed for composite and multi-scale materials contribute to the analysis of complex environments encountered in realistic engineering applications [47].

Spectral–Galerkin-based approaches and Steklov-type eigenvalue problems developed in the context of inverse scattering problems have strengthened the mathematical foundation of resonance-based scattering analyses [48]. New focusing and imaging methods proposed for two-dimensional inverse scattering problems also represent current trends toward more efficient use of scattering data [49].

The concept of fractional-order waves forms an important basis in the physical interpretation of fractional boundary conditions, explaining why phase and amplitude behaviors can be defined more flexibly compared to classical models [50]. Analytical-numerical solutions developed for impedance strips have clearly revealed the effects of boundary conditions on the solution in the case of E-polarization [51]. Finally, studies directly comparing the scattering properties of strip structures with fractional boundary conditions with impedance strips have created an important point of connection in the literature by clearly revealing the relationship between these two approaches [52],[53],[54].

1.3 Contribution of the Thesis

This thesis, offers original contributions to the investigation of electromagnetic scattering problems under more general and flexible boundary conditions for finite and curved geometries. The problems addressed in the dissertation focus on circular strip geometries excited by a line source; the electromagnetic field behavior is analyzed in detail under both classical impedance boundary conditions and fractional boundary

conditions, a generalized form of these conditions. This approach allows for the evaluation of these two boundary condition models, which are mostly considered separately in the literature, within a common framework [25],[26],[52].

The first significant contribution of the dissertation is the systematic investigation of the electromagnetic scattering problem for circular strip geometries with different impedance values on their inner and outer surfaces using an analytical-numerical approach. This makes it possible to model more realistic structures where surface properties change across to the surface, thus moving beyond the classical assumption of uniform impedance.The results obtained clearly demonstrate the effects of surface impedances on resonance frequencies, total radar cross-section, and near-field distributions, providing findings that complement the existing literature [9],[24],[30].

The second and fundamental original contribution of the thesis is the application of fractional boundary conditions to circular strip geometries. While fractional boundary conditions have mostly been considered for planar or semi-infinite geometries in the literature, in this thesis, the fractional boundary condition is applied to a circular strip, which is a curved and finite structure. In this way, a continuous transition between ideal boundary conditions and classical impedance boundary conditions is defined, and it becomes possible to model surface behavior over a wider parameter range [18],[26],[39],[52].

Another important contribution is the detailed investigation of the physical effects of the fractional boundary condition on resonance behavior and field distributions. By changing the fractional order, the effects on the position, width, and amplitude of the resonance peaks are systematically analyzed; The similarities and differences between these behaviors and classical impedance models have been clearly demonstrated. This comparison shows that fractional boundary conditions are not only a mathematical generalization but also offer a physically relevant model [20],[25],[50],[52].

One of the contributions of this thesis to the method is the successful used of the analytic-numeric approach based on orthogonal polynomials under impedance and fractional boundary conditions. This method allows for the accurate acquisition of edge conditions, while enabling the capture of resonance behaviors in finite and curved geometries with high accuracy. Compared with purely numerical methods, physically interpretable solutions have been obtained with lower computation time [3],[4],[25].

Moreover, this thesis examines in detail the effects of source location, aperture size, and surface-related parameters on electromagnetic scattering. Simultaneous evaluation of these parameters under both classical impedance and fractional boundary conditions offers a comprehensive multi-parameter analysis capability, which has been addressed in a limited number of studies in the literature.The findings obtained are directly applicable in terms of the design of resonance controlled structures and tunable scattering elements [27],[30],[43].

Finally, this thesis provides a coherence in the literature thanks to the systematic comparison it establishes between impedance boundary conditions and fractional boundary conditions. The strengths and limitations of both models have been evaluated within the same geometric and numerical framework; thus, a consistent comparison basis has been provided that can serve as a reference for future studies. In this respect, the thesis provides a theoretical and methodological contribution to the treatment of electromagnetic scattering problems under more general boundary conditions [26],[45],[52],[53][54].

2. ELECTROMAGNETIC SCATTERING H-POLARIZED LINE SOURCE BY A DOUBLE-SIDED IMPEDANCE CIRCULAR STRIP

2.1 Formulation of The Problem

The electromagnetic scattering problem discussed in this section is shown in Figure 2.1. The problem is defined using a two-dimensional cylindrical coordinate system (ρ, ϕ) and we assume that there is no variation along the z-axis. Since both the source and scattering field are considered infinite in the z-direction, the analysis is in a two-dimensional case.

The source is provided by an H-polarized line source located at the point (x_0, y_0). The line source represents an electromagnetic source of infinite length along the z-axis and invariant in that direction. This type of modeling reduces the problem to a scalar form by allowing the fields to vary only in the transverse plane.

Figure 2.1 shows a circular strip with a radius a and an angle of 2θ. In cylindrical coordinates, the line source is located at $\overrightarrow{r_0} = (\rho_0, \varphi_0)$, where $\rho_0 = \sqrt{x_0^2 + y_0^2}$. The observation point is $\vec{r} = (\rho, \varphi)$, and the source location on the arc is $\overrightarrow{r'} = (\rho', \varphi')$. The symbols ξ_i for $i = 1,2$ represent the normalized impedances of the outer and inner regions of the circular strip.

Because the circular strip extends infinitely along the z-axis, we can simplify the problem to two dimensions. Therefore, we consider the time dependence given by $e^{-j\omega t}$ but omit it in our analysis to keep things straightforward.

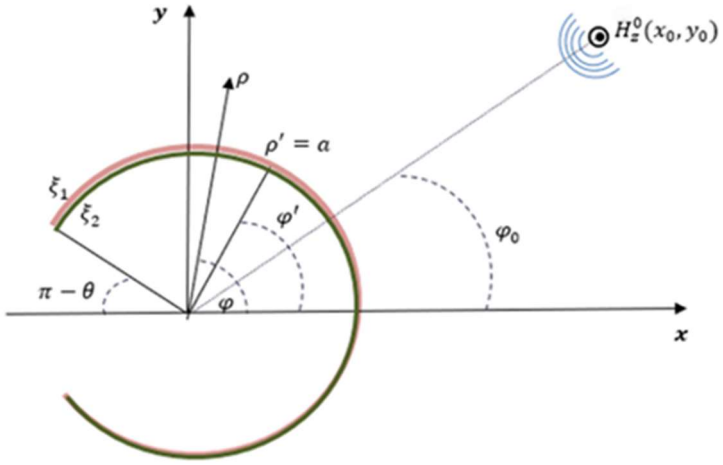

Figure 2.1 : The geometry of the problem.

To find the field components in the region where the scatterer is present, we need to mathematically express both the incident and scattered field components. By applying the appropriate boundary conditions, we can establish the relationship between these fields. The total magnetic field is given by:

$$H_z = H_z^0 + H_z^S \tag{2.1}$$

Here, H_z^0 is the incident field, and H_z^S is the scattered field.

In this context, H_z^0 and H_z^S represent the incident and scattered components of the magnetic field, respectively. The incident magnetic field H_z^0 can be expressed as:

$$H_z^0 = -\mathrm{Z}H_0^{(1)}(k|\vec{r} - \overrightarrow{r_0}|) \tag{2.2}$$

Here, Z is the coefficient, $H_0^{(1)}$ is the Hankel function of the first kind and zero order, k is the wavenumber, and $|\vec{r} - \overrightarrow{r_0}|$ denotes the distance between the observation point and the source point in cylindrical coordinates. Hankel functions are solution of the two-dimensional Helmholtz equation in cylindirical coordinates. The first kind of Hankel function is used for modelling the electromagnetic fields generated by the line sources because it satisfies the condition of a radiating wave at infinity.

In the equation above, Z is defined as $Z = \frac{i\omega\varepsilon_0 A_0}{4}$, where:

ω is the angular frequency measured in s^{-1},

ε_0 is the permittivity of free space measured in $\frac{F}{m}$,

A_0 is line magnetic current amplitude measured in V.

So dimension of Z will be $[Z] = s^{-1}\frac{F}{m}\mathrm{V} = s^{-1}\frac{C/V}{m}\mathrm{V} = \frac{C}{sm} = \frac{A}{m}$

Using the addition theorem the Hankel function (2.2) can expressed as (2.3) [27]:

$$H_0^{(1)}(k|\vec{r}-\vec{r_0}|) = \sum_{m=-\infty}^{\infty} \begin{matrix} J_m(k\rho)H_m^{(1)}(k\rho_0)e^{im(\varphi-\varphi_0)} & \rho \le \rho_0 \\ J_m(k\rho_0)H_m^{(1)}(k\rho)e^{im(\varphi-\varphi_0)} & \rho \ge \rho_0 \end{matrix} \tag{2.3}$$

This leads to the following expression for the incident magnetic field H_z^0 :

$$H_z^0 = -\mathrm{Z} \sum_{m=-\infty}^{\infty} \begin{matrix} J_m(k\rho)H_m^{(1)}(k\rho_0)e^{im(\varphi-\varphi_0)} & \rho \le \rho_0 \\ J_m(k\rho_0)H_m^{(1)}(k\rho)e^{im(\varphi-\varphi_0)} & \rho \ge \rho_0 \end{matrix} \tag{2.4}$$

In this expression:

J_m is the Bessel function of the first kind,

$H_m^{(1)}$ is the Hankel function of the first kind and order m,

$e^{\mathrm{j}m(\varphi-\varphi_0)}$ accounts for the angular dependence between the source and the observation points, ρ and ϕ define the radial and angular coordinates of the observation point, respectively; ρ_0 and ϕ_0 define the position of the line source. This expression allows the incident field to be written analytically in terms of known special functions, thus creating the mathematical structure to which the boundary conditions on the scattering structure will be applied.

Once the expression for the incident field is determined, the total electromagnetic field is obtained by defining the scattered field. The scattered field shows the interaction of the incident wave with the impedance circular strip and is constructed to satisfy the relevant boundary conditions. In this study, the scattered field is expressed through an integral representation using the surface current densities induced on the strip together with the appropriate Green function. By examining the approach presented in studies [27] , [30] and [3], The scattered field can be represented as a convolution of the current densities with Green's function:

$$\vec{H}(\vec{r}) = -i\omega\varepsilon_0\left[1+\frac{1}{k^2}\nabla\nabla\cdot\right]\int G(\vec{r},\overrightarrow{r'})\mu^e(\overrightarrow{r'})\,d\overrightarrow{r'} + \nabla\times\int G(\vec{r},\overrightarrow{r'})\mu^m(\overrightarrow{r'})\,d\overrightarrow{r'} \quad (2.5)$$

For 2D case and magnetic field with z polarization, in cylindrical coordinate system, it simplifies to:

$$H_z^S(\vec{r}) = \int_0^{2\pi}\left\{\mu^m(\varphi') + \mu^e(\varphi')\frac{\partial}{\partial(k\rho')}\right\}H_0^{(1)}\left(k\left|\vec{r}-\overrightarrow{r'}\right|\right)d\varphi', \rho' = a \quad (2.6)$$

Taking derivative with respect to $k\rho'$ made matching between units.

In this equation, $\mu^m(\varphi')$ and $\mu^e(\varphi')$ represent the magnetic and electric current densities, respectively. The function $H_0^{(1)}$ in equation (2.6) is the Hankel function of the first kind and order zero, and $\rho' = a$ indicates that the integration is performed along the circular strip at radius a.

$H_0^{(1)}\left(k\left|\vec{r}-\overrightarrow{r'}\right|\right)$ in this integral is function of only φ variable because ρ' is fixed.

To apply the boundary conditions, we need to define the final expression for the scattered field for which again we use the adition theorem [27,30]. As a result we get the equation (2.7) :

$$H_0^{(1)}\left(k\left|\vec{r}-\overrightarrow{r'}\right|\right) = \begin{cases}\sum_{n=-\infty}^{\infty} j_n(k\rho)H_n^{(1)}(k\rho')e^{in(\varphi-\varphi')}\rho \le a \\ \sum_{n=-\infty}^{\infty} j_n(k\rho')H_n^{(1)}(k\rho)e^{in(\varphi-\varphi')}\rho \ge a\end{cases} \quad (2.7)$$

In equation (2.8) we use the Fourier transform for the electric and magnetic current densities:

$$\mu^e(\varphi') = \frac{2i}{\pi\varepsilon}\sum_{m=-\infty}^{\infty}\mu^e{}_m e^{im\varphi'} = \sum_{m=-\infty}^{\infty}\hat{\mu}_m^e e^{im\ '}$$
$$\mu^m(\varphi') = \frac{2i}{\pi\varepsilon}\sum_{m=-\infty}^{\infty}\mu^m{}_m e^{im\varphi'} = \sum_{m=-\infty}^{\infty}\hat{\mu}_m^m e^{im\varphi'}$$

$$\hat{\mu}_m^e = \frac{1}{2\pi}\int_{-\theta}^{\theta}\mu^e(\varphi)e^{-im\varphi}d\varphi \quad (2.8)$$
$$\hat{\mu}_m^m = \frac{1}{2\pi}\int_{-\theta}^{\theta}\mu^m(\varphi)e^{-im\varphi}d\varphi$$

Equation (2.9) shows the scattered magnetic field as a contour integral by substituting the hankel function using the addition theorem:

$$H_z^S(\vec{r}) = \int_0^{2\pi} \left\{ \sum_{m=-\infty}^{\infty} \hat{\mu}_m^m e^{im\varphi'} + \sum_{m=-\infty}^{\infty} \hat{\mu}_m^e e^{im\varphi'} \frac{\partial}{\partial(k\rho')} \right\} \begin{cases} \sum_{n=-\infty}^{\infty} j_n(k\rho) H_n^{(1)}(k\rho') e^{in(\varphi-\varphi')} \rho \le a \\ \sum_{n=-\infty}^{\infty} j_n(k\rho') H_n^{(1)}(k\rho) e^{in(\varphi-\varphi')} \rho \ge a \end{cases} d\varphi', \rho' = a \tag{2.9}$$

After putting (2.8) in (2.9) we obtain equation (2.10):

$$H^s = \sum_{m=-\infty}^{\infty} \hat{\mu}_m^m \begin{cases} \sum_{n=-\infty}^{\infty} j_n(k\rho) H_n^{(1)}(k\rho') \int_0^{2\pi} e^{im\varphi'} e^{in(\varphi-\varphi')} d\varphi' \; \rho \le a, \rho' = a \\ \sum_{n=-\infty}^{\infty} j_n(k\rho') H_n^{(1)}(k\rho) \int_0^{2\pi} e^{im\varphi'} e^{in(\varphi-\varphi')} d\varphi' \; \rho \ge a, \rho' = a \end{cases} +$$

$$+ \sum_{m=-\infty}^{\infty} \hat{\mu}_m^e \frac{\partial}{\partial(k\rho')} \begin{cases} \sum_{n=-\infty}^{\infty} j_n(k\rho) H_n^{(1)}(k\rho') \int_0^{2\pi} e^{im\varphi'} e^{in(\varphi-\varphi')} d\varphi' \; \rho \le a, \rho' = a \\ \sum_{n=-\infty}^{\infty} j_n(k\rho') H_n^{(1)}(k\rho) \int_0^{2\pi} e^{im\varphi'} e^{in(\varphi-\varphi')} d\varphi' \; \rho \ge a, \rho' = a \end{cases} \tag{2.10}$$

Using the next formula $\delta_{mn} = \frac{1}{2\pi}\int_0^{2\pi} e^{i(m-n)\varphi'} d\varphi'$, $\varepsilon = ka$ and taking derivative we get the final expression for the scattered field z component :

$$H_z^S = \frac{4i}{\varepsilon} \sum_{m=-\infty}^{\infty} \hat{\mu}_m^m \begin{cases} J_m(k\rho) H_m^{(1)}(\varepsilon) e^{im\varphi'} \; \rho \le a \\ J_m(\varepsilon) H_m^{(1)}(k\rho) e^{im\varphi'} \; \rho \ge a \end{cases} + \frac{4i}{\varepsilon} \sum_{m=-\infty}^{\infty} \hat{\mu}_m^e \begin{cases} J_m(k\rho) H_m^{(1)'}(\varepsilon) e^{im\varphi'} \; \rho \le a \\ J_m'(\varepsilon) H_m^{(1)}(k\rho) e^{im\varphi'} \; \rho \ge a \end{cases} \tag{2.11}$$

where $\varepsilon = ka$.

By considering the edge conditions and the geometry of the problem, we can express the current densities as:

$$\mu^e(\eta) = (1-\eta^2)^{\nu_1} \sum_{n=0}^{\infty} x_n C_n^{\nu_1+\frac{1}{2}}(\eta),$$
$$\mu^m(\eta) = (1-\eta^2)^{\nu_2} \sum_{n=0}^{\infty} x_n C_n^{\nu_2+\frac{1}{2}}(\eta), \tag{2.12}$$

To satisfy the edge conditions, we set ν_1 and ν_2 are set to -1/2 and 1/2, as suggested in reference [31]. Here, $C_n^{\nu_1+\frac{1}{2}}(\eta)$ are the Gegenbauer polynomials. According to reference [30], the Fourier coefficients in equation (2.8) are given by:

$$\hat{\mu}_m^e = \frac{\theta}{\Gamma\left(\nu_1+\frac{1}{2}\right)} \sum_{n=0}^{\infty} i^n x_n \beta_n^{\nu_1+\frac{1}{2}} \frac{J_{\nu_1+n+\frac{1}{2}}(-m\theta)}{(-2m\theta)^{\left(\nu_1+\frac{1}{2}\right)}},$$
$$\hat{\mu}_m^m = \frac{\theta}{\Gamma\left(\nu_2+\frac{1}{2}\right)} \sum_{n=0}^{\infty} i^n y_n \beta_n^{\nu_2+\frac{1}{2}} \frac{J_{\nu_2+n+\frac{1}{2}}(-m\theta)}{(-2m\theta)^{\left(\nu_2+\frac{1}{2}\right)}}, \tag{2.13}$$

where:

- $\beta_n^{\nu_i+\frac{1}{2}} = \frac{\Gamma(2\nu_i+1+n)}{\Gamma(n+1)}$, for $i = 1,2$
- Γ is the Gamma function,
- m is the harmonic order,
- i is the imaginary unit.

By substituting the expressions for $\hat{\mu}_m^e$ and $\hat{\mu}_m^m$ back into the expression for the scattered field H_z^S (2.11) and applying the boundary conditions (2.15) discussed below, we can solve for the unknown coefficients x_n and y_n. This leads to a complete solution for the scattered field, satisfying both the edge conditions and the geometry of the problem.

To simplify the equations and reach to the normalization, we submit a change of variable by defining $\eta = \frac{\varphi}{\theta}$, which means that $\varphi = \theta\eta$. This substitution is helpful

because Gegenbauer polynomials are defined in the interval $[-1,1]$, and this change guide us to find our angular variable into that range.

After deriving the mathematical expressions for the incident field, scattered field, and current densities, we can use the Leontovich boundary condition (also named as the impedance boundary condition). This boundary condition is given by:

$$\frac{\partial}{\partial k\rho} H_z \pm ik\xi_{1,2} H_z = 0, \rho = a \tag{2.14}$$

Here, $\xi_{1,2}$ shows the normalized impedances of the outer and inner surfaces of the circular strip, and the $\pm$ sign corresponds to the direction of the normal vector on the boundary. So we need to apply this condition inside and outside of the circular arc.

Here we have to consider 2 cases. First $\rho_0 < a$ and then $\rho_0 > a$

Let's first consider the case $\rho_0 < a$:

In this case the Leontovich boundary condition will be:

$$\frac{\partial}{\partial k\rho} H_z + ik\xi_1 H_z = 0, \rho = a^+$$

Inseting the expression of total field H_z from (2.1) and taking derivative we get:

$$\frac{4\mathrm{i}}{\varepsilon} \sum_{m=-\infty}^{\infty} \bar{\bar{\mu}}_m^m J_m(\varepsilon) \widetilde{H}_m^{(1)} e^{\mathrm{i}m\varphi'} + \frac{4i}{\varepsilon} \sum_{m=-\infty}^{\infty} \bar{\bar{\mu}}_m^e J'_m(\varepsilon) \widetilde{H}_m^{(1)} e^{\mathrm{i}m\varphi'} = \mathrm{Z} \sum_{m=-\infty}^{\infty} J_m(k\rho_0) \widetilde{H}_m^{(1)} e^{\mathrm{i}m(\varphi' - \varphi_0)} \tag{2.15}$$

in this equation:

- $\tilde{J}_m = J'_m(\varepsilon) + \mathrm{i}k\xi_1 J_m(\varepsilon)$
- $\widetilde{H}_m^{(1)} = H_m^{(1)\prime}(\varepsilon) + \mathrm{i}k\xi_1 H_m^{(1)}(\varepsilon)$
- $\bar{\bar{\mu}}_m^e = \hat{\mu}_m^e \frac{\pi\varepsilon}{2i}$
- $\bar{\bar{\mu}}_m^m = \hat{\mu}_m^m \frac{\pi\varepsilon}{2i}$

Here, $\varepsilon = ka, J_m$ and $H_m^{(1)}$ are Bessel and Hankel functions of the first kind of order m, and primes denote derivatives with respect to the argument.

If we put expressions of $\hat{\mu}_m^e$ and $\hat{\mu}_m^m$ from equation (2.13) into (2.15) we get:

$$2\pi \sum_{m=-\infty}^{\infty} \left(\frac{\theta}{\Gamma\left(\nu_2 + \frac{1}{2}\right)} \sum_{n=0}^{\infty} i^n y_n \beta_n^{\nu_2+\frac{1}{2}} \frac{J_{\nu_2+n+\frac{1}{2}}(-m\theta)}{(-2m\theta)^{\left(\nu_2+\frac{1}{2}\right)}} \right) J_m(\varepsilon) \widetilde{H}_m^{(1)} e^{im\varphi'}$$
$$+ 2\pi \sum_{m=-\infty}^{\infty} \left(\frac{\theta}{\Gamma\left(\nu_1 + \frac{1}{2}\right)} \sum_{n=0}^{\infty} i^n x_n \beta_n^{\nu_1+\frac{1}{2}} \frac{J_{\nu_1+n+\frac{1}{2}}(-m\theta)}{(-2m\theta)^{\left(\nu_1+\frac{1}{2}\right)}} \right) J'_m(\varepsilon) \widetilde{H}_m^{(1)} e^{im\varphi'} \quad (2.16)$$
$$= \mathrm{Z} \sum_{m=-\infty}^{\infty} J_m(k\rho_0) \widetilde{H}_m^{(1)} e^{im\ '} e^{-im\varphi_0}$$

Now for this expression:

- Γ denotes the Gamma function.
- $\beta_n^{\nu_1+\frac{1}{2}} = \frac{\Gamma(2\nu_i+1+n)}{\Gamma(n+1)}$ for $i = 1,2$.
- x_n and y_n are coefficients of the current densities.
- $\nu_1 = -\frac{1}{2}$ and $\nu_2 = \frac{1}{2}$, we chose these values to satisfy the edge conditions.
- θ is half the angular width of the circular strip.
- J_α is the Bessel function of the first kind of order α.

To simplify the expression and ensure faster convergence of the system of equations, we expand the exponential term $e^{\mathrm{j}m\varphi'}$ using the following series:

$$e^{im\varphi'} = \left(\frac{2}{m\theta}\right)^{\nu+\frac{1}{2}} \Gamma(\nu + \frac{1}{2}) \sum_{k=0}^{\infty} i^k \left(k + \nu + \frac{1}{2}\right) J_{k+\nu+\frac{1}{2}}(m\theta) C_k^{\nu+\frac{1}{2}}(\eta) \quad (2.17)$$

Here:

- ν is a parameter related to the edge condition ($\nu = \nu_1 \ or \ \nu_2$).
- $C_k^{\nu+\frac{1}{2}}(\eta)$ are the Gegenbauer polynomials.
- $\eta = \frac{\varphi'}{\theta}$ is a normalized angular variable, mapping φ' into the interval $[-1,1]$ because Gegenbauer polynomials are defined on this interval.
- $J_\alpha(m\theta)$ is the Bessel function of order α evaluated at $m\theta$.

- $\Gamma(\nu+\frac{1}{2})$ is the Gamma function

By incorporating this expansion, we rewrite equation (2.16) in a more compact form, which helps in solving the system of linear algebraic equations efficiently. This will improve convergence and it will reduce computational work.

In the expressions given above, the variable and function definitions have been rearranged to conform to the notation used in this study. The gamma function $\Gamma(z)$ represents the analytic extension of the factorial function into the complex plane. The Bessel and Hankel functions are the principal solutions of the Bessel differential equation and are used in wave propagation problems with cylindrical symmetry.

By substituting (2.17) expansion into equation (2.16), a system of linear algebraic equations is obtained for the unknown coefficients x_p and y_p:

$$2\pi\frac{\theta}{\Gamma\left(\nu_2+\frac{1}{2}\right)}\sum_{n=0}^{\infty} i^p x_p \beta_p^{\nu_2+\frac{1}{2}}\tilde{Q}_{kp}^{11}+2\pi\frac{\theta}{\Gamma\left(\nu_1+\frac{1}{2}\right)}\sum_{p=0}^{\infty} i^p y_p \beta_p^{\nu_2+\frac{1}{2}}\tilde{Q}_{kp}^{12}=\tilde{A}_k^1 \qquad (2.18)$$

where:

$$\tilde{Q}_{kp}^{11}=\sum_{m=-\infty}^{\infty} J_m(\varepsilon)\tilde{H}_m^{(1)}\left(\frac{2}{m\theta}\right)^{\nu_1+\frac{1}{2}}\Gamma(\nu_1+\frac{1}{2})\,J_{k+\nu_1+\frac{1}{2}}(m\theta)\frac{J_{\nu_2+n+\frac{1}{2}}(-m\theta)}{(-2m\theta)^{\left(\nu_2+\frac{1}{2}\right)}}$$

$$\tilde{Q}_{kp}^{12}=\sum_{m=-\infty}^{\infty} J'_m(\varepsilon)\tilde{H}_m^{(1)}\left(\frac{2}{m\theta}\right)^{\nu_1+\frac{1}{2}}\Gamma(\nu_1+\frac{1}{2})\,J_{k+\nu_1+\frac{1}{2}}(m\theta)\frac{J_{\nu_1+n+\frac{1}{2}}(-m\theta)}{(-2m\theta)^{\left(\nu_1+\frac{1}{2}\right)}}$$

$$\tilde{A}_k^1=\mathrm{Z}\sum_{m=-\infty}^{\infty} J_m(k\rho_0)\tilde{H}_m^{(1)}\left(\left(\frac{2}{m\theta}\right)^{\nu_1+\frac{1}{2}}\Gamma(\nu_1+\frac{1}{2})\,J_{k+\nu_1+\frac{1}{2}}(m\theta)\right)e^{-im\varphi_0}$$

When the same approach is applied to the inner surface, the impedance boundary condition on this surface is determined as follows:

$$\left(\frac{\partial}{\partial k\rho}H_z-ik\xi_2 H_z=0,\rho=a^-\right)$$

In this case, instead of (2.15) we get:

$$-\mathrm{Z}\sum_{m=-\infty}^{\infty} J_m(k\rho_0)\widetilde{H}_{m1}e^{im(\varphi'-\varphi_0)} + \frac{4i}{\varepsilon}\sum_{m=-\infty}^{\infty}\bar{\bar{\mu}}_m^m H_m^{(1)}(\varepsilon)\tilde{J}_{m1}e^{im\varphi'} + \frac{4i}{\varepsilon}\sum_{m=-\infty}^{\infty}\bar{\bar{\mu}}_m^e H_m^{(1)\prime}(\varepsilon)\tilde{J}_{m1}e^{im\varphi'} = 0 \quad (2.19)$$

where,

$\tilde{J}_{m1} = J_m'(\varepsilon) - ik\xi_2 J_m(\varepsilon)$ and $\widetilde{H}_{m1} = H_m^{(1)\prime}(\varepsilon) - ik\xi_2 H_m^{(1)}(\varepsilon)$.

By expressing again the current densities using Fourier transform the following equations are obtained:

$$2\pi\frac{\theta}{\Gamma\left(\nu_2+\frac{1}{2}\right)}\sum_{p=0}^{\infty} i^p y_p \beta_n^{\nu_2+\frac{1}{2}}\tilde{Q}_{kp}^{21} + 2\pi\frac{\theta}{\Gamma\left(\nu_1+\frac{1}{2}\right)}\sum_{p=0}^{\infty} i^p x_p \beta_p^{\nu_1+\frac{1}{2}}\tilde{Q}_{kp}^{22} = \tilde{A}_k^2 \quad (2.20)$$

Where:

$$\tilde{Q}_{kp}^{21} = \sum_{m=-\infty}^{\infty} H_m^{(1)}(\varepsilon)\tilde{J}_{m1}\left(\frac{2}{m\theta}\right)^{\nu_1+\frac{1}{2}}\Gamma(\nu_1+\frac{1}{2})\,J_{k+\nu_1+\frac{1}{2}}(m\theta)\frac{J_{\nu_2+p+\frac{1}{2}}(-m\theta)}{(-2m\theta)^{\left(\nu_2+\frac{1}{2}\right)}}$$

$$\tilde{Q}_{kp}^{22} = \sum_{m=-\infty}^{\infty} H_m^{(1)\prime}(\varepsilon)\tilde{J}_{m1}\left(\frac{2}{m\theta}\right)^{\nu_1+\frac{1}{2}}\Gamma(\nu_1+\frac{1}{2})\,J_{k+\nu_1+\frac{1}{2}}(m\theta)\frac{J_{\nu_1+p+\frac{1}{2}}(-m\theta)}{(-2m\theta)^{\left(\nu_1+\frac{1}{2}\right)}}$$

$$\tilde{A}_k^2 = \mathrm{Z}\sum_{m=-\infty}^{\infty} J_m(k\rho_0)\widetilde{H}_{m1}\left(\left(\frac{2}{m\theta}\right)^{\nu_1+\frac{1}{2}}\Gamma(\nu_1+\frac{1}{2})\,J_{k+\nu_1+\frac{1}{2}}(m\theta)\right)e^{-im\varphi_0}$$

Solving this related system of equations yields the coefficients x_p and y_p, which describe the induced current distribution on the circular strip. After determining these coefficients, the scattered field can be calculated with (2.11), and the electromagnetic scattering behavior of the structure can be examined in detail.

When m=0 we get the devision by 0 in (2.13) and in the expressions of $\tilde{Q}_{kp}^{11}$, $\tilde{Q}_{kp,}^{12}$ $\widetilde{Q}_{kp}^{21}$, $\widetilde{\tilde{Q}_{kp,}^{22}}$ A_k^1 and $\widetilde{A}_k^2$ So this case should be considered seperately. For this we express the Bessel function as a series and such a way we eliminate devision by 0. As a result we can express Fourier coefficients for m=0 case:

$$\mu_m^e(m=0)=\frac{\pi\varepsilon}{2i}\theta x_0\frac{1}{4^{\left(\nu_1+\frac{1}{2}\right)}}\frac{\Gamma(2\nu_1+1)}{\Gamma(\nu_1+\frac{3}{2})\Gamma\left(\nu_1+\frac{1}{2}\right)}$$
$$\mu_m^m(m=0)=\frac{\pi\varepsilon}{2i}\theta x_0\frac{1}{4^{\left(\nu_2+\frac{1}{2}\right)}}\frac{\Gamma(2\nu_2+1)}{\Gamma(\nu_2+\frac{3}{2})\Gamma\left(\nu_2+\frac{1}{2}\right)} \quad (2.21)$$

and:

$$\tilde{Q}_{kp}^{11}(m=0,k=0,p=0)=J_m(\varepsilon)\tilde{H}_m^{(1)}\left(\frac{1}{4}\right)^{\nu_2+\frac{1}{2}}\left(\frac{\Gamma(\nu_1+\frac{1}{2})}{\Gamma(\nu_1+\frac{3}{2})\Gamma(\nu_2+\frac{3}{2})}\right)$$

$$\tilde{Q}_{kp}^{12}(m=0,p=0,q=0)=J_m'(\varepsilon)\tilde{H}_m^{(1)}\frac{1}{4^{\left(\nu_1+\frac{1}{2}\right)}}\left(\frac{\Gamma(\nu_1+\frac{1}{2})}{\Gamma(\nu_1+\frac{3}{2})\Gamma(\nu_1+\frac{3}{2})}\right)$$

$$\tilde{Q}_{kp}^{21}(m=0,k=0,p=0)=H_m^{(1)}(\varepsilon)\tilde{J}_{m1}\frac{\Gamma(\nu_1+\frac{1}{2})}{\Gamma(\nu_1+\frac{3}{2})\Gamma(\nu_2+\frac{3}{2})}\frac{1}{4^{\nu_2+\frac{1}{2}}}$$

$$\tilde{Q}_{kp}^{22}(m=0,p=0,q=0)=H_m^{(1)\prime}(\varepsilon)\tilde{J}_{m1}\frac{1}{4^{\nu_1+\frac{1}{2}}}\frac{\Gamma(\nu_1+\frac{1}{2})}{\Gamma(\nu_1+\frac{3}{2})\Gamma(\nu_1+\frac{3}{2})}$$

$$\tilde{A}_k^1(m=0,k=0)=\mathrm{Z}J_m(k\rho_0)\tilde{H}_m^{(1)}\left(\frac{1}{(\nu_1+\frac{1}{2})}\right)$$

$$\tilde{A}_k^2=\mathrm{Z}\sum_{m=-\infty}^{\infty}J_m(k\rho_0)\tilde{H}_{m1}\left(\left(\frac{2}{m\theta}\right)^{\nu_1+\frac{1}{2}}\Gamma(\nu_1+\frac{1}{2})\,J_{k+\nu_1+\frac{1}{2}}(m\theta)\right)e^{-im\varphi_0}$$

After that we can do similar procedures when $\rho_0 > a$

We get the analog of the linear algebraic equation system (2.18):

$$2\pi\frac{\theta}{\Gamma\left(\nu_2+\frac{1}{2}\right)}\sum_{n=0}^{\infty}i^p x_p\beta_p^{\nu_2+\frac{1}{2}}\tilde{Q}_{kp}^{11}+2\pi\frac{\theta}{\Gamma\left(\nu_1+\frac{1}{2}\right)}\sum_{p=0}^{\infty}i^p y_p\beta_p^{\nu_2+\frac{1}{2}}\tilde{Q}_{kp}^{12}=\tilde{A}_k^1$$
$$2\pi\frac{\theta}{\Gamma\left(\nu_2+\frac{1}{2}\right)}\sum_{p=0}^{\infty}i^p y_p\beta_n^{\nu_2+\frac{1}{2}}\tilde{Q}_{kp}^{21}+2\pi\frac{\theta}{\Gamma\left(\nu_1+\frac{1}{2}\right)}\sum_{p=0}^{\infty}i^p x_p\beta_p^{\nu_1+\frac{1}{2}}\tilde{Q}_{kp}^{22}=\tilde{A}_k^2 \quad (2.22)$$

where:

$$\tilde{Q}_{kp}^{11} = J_m(\varepsilon)\tilde{H}_m^{(1)}\left(\frac{2}{m\theta}\right)^{\nu_1+\frac{1}{2}}\Gamma(\nu_1+\frac{1}{2})\,J_{k+\nu_1+\frac{1}{2}}(m\theta)\frac{J_{\nu_2+n+\frac{1}{2}}(-m\theta)}{(-2m\theta)^{\left(\nu_2+\frac{1}{2}\right)}}$$

$$\tilde{Q}_{kp}^{12} = \sum_{m=-\infty}^{\infty} J_m'(\varepsilon)\tilde{H}_m^{(1)}\left(\frac{2}{m\theta}\right)^{\nu_1+\frac{1}{2}}\Gamma(\nu_1+\frac{1}{2})\,J_{k+\nu_1+\frac{1}{2}}(m\theta)\frac{J_{\nu_1+n+\frac{1}{2}}(-m\theta)}{(-2m\theta)^{\left(\nu_1+\frac{1}{2}\right)}}$$

$$\tilde{A}_k^1 = \mathrm{Z}\sum_{m=-\infty}^{\infty}\tilde{J}_m H_m^{(1)}(k\rho_0)\left(\left(\frac{2}{m\theta}\right)^{\nu_1+\frac{1}{2}}\Gamma(\nu_1+\frac{1}{2})\,J_{k+\nu_1+\frac{1}{2}}(m\theta)\right)e^{-im\varphi_0}$$

$$\tilde{Q}_{kp}^{21} = H_m^{(1)}(\varepsilon)\tilde{J}_{m1}\left(\frac{2}{m\theta}\right)^{\nu_1+\frac{1}{2}}\Gamma(\nu_1+\frac{1}{2})\,J_{k+\nu_1+\frac{1}{2}}(m\theta)\frac{J_{\nu_2+p+\frac{1}{2}}(-m\theta)}{(-2m\theta)^{\left(\nu_2+\frac{1}{2}\right)}}$$

$$\tilde{Q}_{kp}^{22} = \sum_{m=-\infty}^{\infty} H_m^{(1)\prime}(\varepsilon)\tilde{J}_{m1}\left(\frac{2}{m\theta}\right)^{\nu_1+\frac{1}{2}}\Gamma(\nu_1+\frac{1}{2})\,J_{k+\nu_1+\frac{1}{2}}(m\theta)\frac{J_{\nu_1+p+\frac{1}{2}}(-m\theta)}{(-2m\theta)^{\left(\nu_1+\frac{1}{2}\right)}}$$

$$\tilde{A}_k^2 = \mathrm{Z}\sum_{m=-\infty}^{\infty}\tilde{J}_{m1} H_m^{(1)}(k\rho_0)\left(\left(\frac{2}{m\theta}\right)^{\nu_1+\frac{1}{2}}\Gamma(\nu_1+\frac{1}{2})\,J_{k+\nu_1+\frac{1}{2}}(m\theta)\right)e^{-im\varphi_0}$$

$$\tilde{J}_m = J_m'(\varepsilon) + ik\xi_1 J_m(\varepsilon)$$

$$\tilde{H}_m^{(1)} = H_m^{(1)\prime} + ik\xi_1 H_m^{(1)}(\varepsilon)$$

$$\tilde{J}_{m1} = J_m'(\varepsilon) - ik\xi_2 J_m(\varepsilon)$$

Again for m=0 case:

$$\mu_m^e(m=0) = \frac{\pi\varepsilon}{2i}\theta x_0\frac{1}{4^{\left(\nu_1+\frac{1}{2}\right)}}\frac{\Gamma(2\nu_1+1)}{\Gamma(\nu_1+\frac{3}{2})\Gamma\left(\nu_1+\frac{1}{2}\right)}$$

$$\mu_m^m(m=0) = \frac{\pi\varepsilon}{2i}\theta x_0\frac{1}{4^{\left(\nu_2+\frac{1}{2}\right)}}\frac{\Gamma(2\nu_2+1)}{\Gamma(\nu_2+\frac{3}{2})\Gamma\left(\nu_2+\frac{1}{2}\right)}$$

and:

$$\tilde{Q}_{kp}^{12}(m=0,p=0,q=0)=J_m'(\varepsilon)\tilde{H}_m^{(1)}\frac{1}{4^{\left(\nu_1+\frac{1}{2}\right)}}\left(\frac{\Gamma(\nu_1+\frac{1}{2})}{\Gamma(\nu_1+\frac{3}{2})\Gamma(\nu_1+\frac{3}{2})}\right)$$

$$\tilde{Q}_{kp}^{21}(m=0,k=0,p=0)=H_m^{(1)}(\varepsilon)\tilde{J}_{m1}\frac{\Gamma(\nu_1+\frac{1}{2})}{\Gamma(\nu_1+\frac{3}{2})\Gamma(\nu_2+\frac{3}{2})}\frac{1}{4^{\nu_2+\frac{1}{2}}}$$

$$\tilde{Q}_{kp}^{11}(m=0,k=0,p=0)=J_m(\varepsilon)\tilde{H}_m^{(1)}\left(\frac{1}{4}\right)^{\nu_2+\frac{1}{2}}\left(\frac{\Gamma(\nu_1+\frac{1}{2})}{\Gamma(\nu_1+\frac{3}{2})\Gamma(\nu_2+\frac{3}{2})}\right)$$

$$\tilde{Q}_{kp}^{22}(m=0,p=0,q=0)=H_m^{(1)'}(\varepsilon)\tilde{J}_{m1}\frac{1}{4^{\nu_1+\frac{1}{2}}}\frac{\Gamma(\nu_1+\frac{1}{2})}{\Gamma(\nu_1+\frac{3}{2})\Gamma(\nu_1+\frac{3}{2})}$$

$$\tilde{A}_k^1(m=0,k=0)=\mathrm{Z}H_m^{(1)}(k\rho_0)\tilde{J}_m\left(\frac{1}{(\nu_1+\frac{1}{2})}\right)$$

$$\tilde{A}_k^2(m=0,k=0)=\mathrm{Z}H_m^{(1)}(k\rho_0)\tilde{J}_{m1}\left(\frac{1}{(\nu_1+\frac{1}{2})}\right)$$

In this section, the scattering problem corresponding to the interaction of an H-polarized line source with a circular strip is formulated. The representations of the incident and scattered fields are clearly defined, and a linear algebraic equation is obtained by applying boundary conditions. The use of orthogonal polynomial expansions and consideration of edge conditions provides fast convergence and high computational correctness.

This mathematical structure forms the basis for calculating the numerical results that will be presented in the next section.

2.2 Numerical Results and the Comparison

This section presents the obtained numerical results and their comparisons. The analysis is primarily carried out using the Total Radar Cross Section (TRCS) and its corresponding near-field distributions; this approach is also mentioned in [32]. TRCS is defined as the integral of the scattered radar cross-section angularly across all

observation directions, representing a general measure of the electromagnetic wave scattered by the structure.

The calculations are examined numerically, the effects of fundamental parameters such as the position of the line source (inside or outside the circular strip), wave number, aperture size, and impedance values assigned to the inner and outer surfaces of the circular arc on the scattering behavior are investigated, and the electromagnetic scattering characteristics of the structure are comprehensively analyzed by systematically changing these parameters.

2.2.1 Numerical results

In this section, we present the results of the total radar cross-section (TRCS) and near-field distributions for the different variables mentioned above.

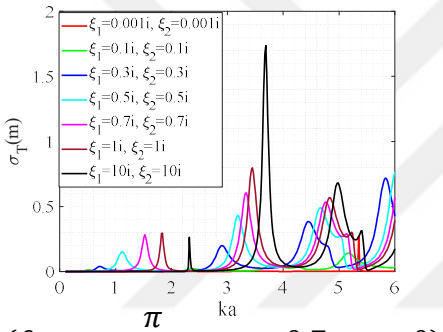

$(\theta = \pi - \frac{\pi}{10}, x_0 = -0.7, y_0 = 0)$

(a)

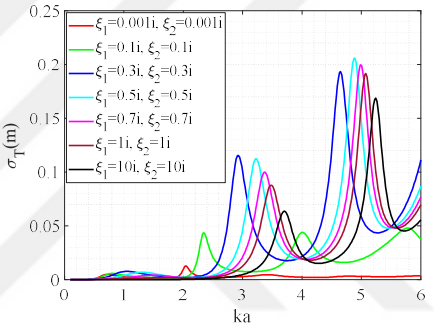

$(\theta = \pi - \frac{\pi}{3}, x_0 = 0, y_0 = 0.7)$

(b)

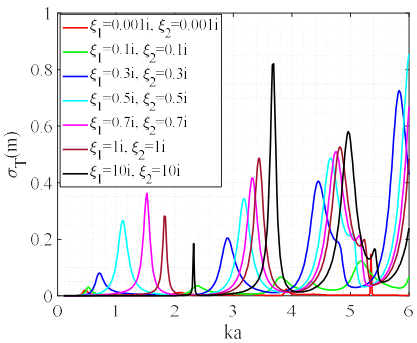

$\theta = \pi - \frac{\pi}{10}, x_0 = 0.7, y_0 = 0)$

(c)

Figure 2.2 : TRCS for the line source is located inside for different impedance values ranging from PEC to PMC in the limit cases $(a = 1)$.

Figure 2.2(a) demonstrates a non-monotonic behavior in the first resonance, whereas both the second and third resonances exhibit a clear and consistent monotonic increase.

As expected, the resonance values increase as we approach the perfectly matched conductor (PMC) surface for each mode.

In the specific case where $\theta = \pi - \frac{\pi}{10}$ (Figure 2.2(a)), we observe remarkably sharp and distinguishable resonances. Increasing the impedance value leads to a shift of the resonance frequency to a higher frequency.

However, in the case of Figure 2.2(b), both the first and second resonances exhibit non-monotonic behavior.

It is worth noting that at the highest point, for the first resonance value for both ξ_1 and ξ_2 is equal to $0.3i$ and for the second resonance is $0.5i$. These observations suggests that the system functions as a better resonator between a perfectly electric conductor (PEC) and a perfectly magnetic conductor (PMC), and it corresponds to a real material scenario.

Moving on to Figure 2.2(c), we observe that the first resonance does not exhibit a monotonic pattern, but the maximum point at the first resonance occurs when $\xi_1 = \xi_2 = 0.7i$. However, both the second and third resonances display clear and consistent monotonic behavior. By increasing the impedance value, the resonance frequency is shifted to a higher frequency.

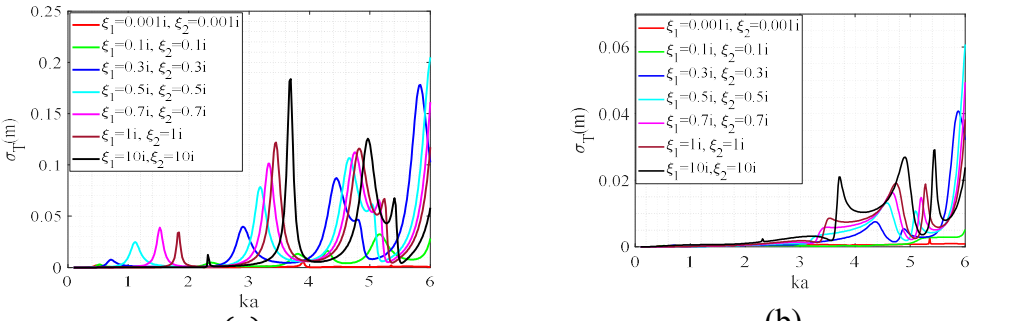

(a)

$(\theta = \pi - \frac{\pi}{10}, x_0 = -1.5, y_0 = 0)$

(b)

$(\theta = \pi - \frac{\pi}{10}, x_0 = 1.5, y_0 = 0)$

Figure 2.3 : TRCS for the line source is located outside for different impedance values ranging from PEC to PMC in the limit cases $(a = 1)$.

Figure 2.3(a) exhibits a non-monotonic behavior in the first resonance, reaching its maximum resonance value when $\xi_1 = \xi_2 = 0.7i$. Increasing the impedance value

leads to a shift of the resonance frequency to a higher value. Additionally, a consistent and monotonic increase is observed in both the second and third resonances.

Moving on to Figure 2.3(b), we observe a consistent and gradual increase across the first, second, and third resonances. Similar to the previous case, increasing the impedance value results in a higher resonance frequency.

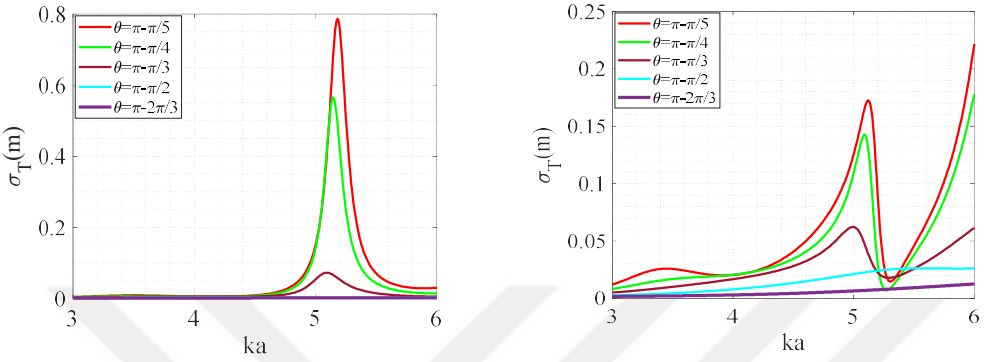

(a)
$(\xi_1 = \xi_2 = 1i, x_0 = 0.01, y_0 = 0)$

(b)
$(\xi_1 = \xi_2 = 1i, x_0 = 0.7, y_0 = 0)$

Figure 2.4 : TRCS for the line source is located inside for different aperture sizes while other parameters are constant $(a = 1)$.

In Figure 2.4(a), there is a direct relationship between the increase in the theta angle and the corresponding decrease in resonance. As the theta angle increases, the resonance values decrease. This pattern indicates a clear inverse correlation between the two variables.

Figure 2.4(b) shows a clear pattern of monotonic decrease in resonance. Because of resonance levels decrease smoothly and continuously, we can say that a change in the relevant parameter leads to a systematic reducing of resonance intensity.

When the ξ_2 parameter is kept constant and the ξ_1 value is changed, we observed resonance peak amplitudes decrease compared to cases corresponding to higher ξ_1 values. This shows that the ξ_1 parameter has a direct effect on resonance peak amplitudes.

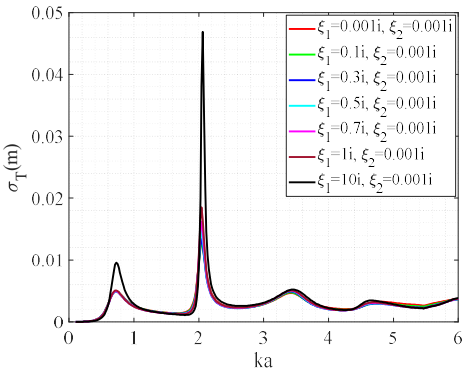

(a)

$(\theta = \pi - \frac{\pi}{3}, x_0 = 0, y_0 = 0.7)$

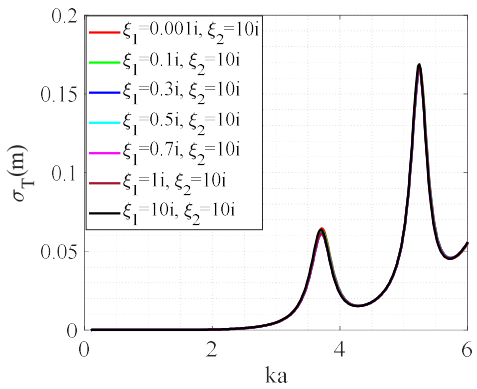

(b)

$(\theta = \pi - \frac{\pi}{3}, x_0 = 0, y_0 = 0.7)$

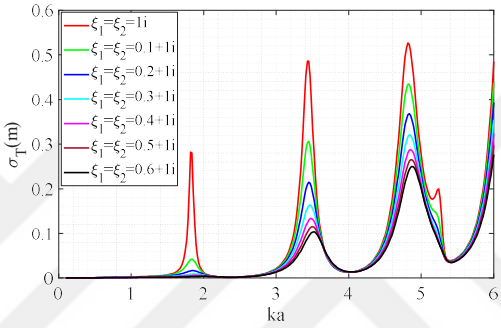

(c)

$(\theta = \pi - \frac{\pi}{10}, x_0 = 0.7, y_0 = 0)$

Figure 2.5 : TRCS for the line source and it's located inside $(a = 1)$.

In Figures 2.5(a) and (b), it is observed that when the ξ_2 parameter is kept constant and close to the PEC limit, the resonance amplitude decreases with increasing ξ_1. This trend shows that the change in the ξ_1 parameter has a decisive effect on the resonance intensity and leads to a decrease in the resonance amplitude.

In contrast, when the $\xi 2$ parameter is kept constant and close to the PMC limit in Figure 2.5(b), it is observed that the resonance amplitudes take very close values to each other and are clustered in a narrow range.

By examining these graphs, we can see that the parameters ξ_1 and ξ_2 , they are not important to determine the resonance characteristics.

Figure 2.5(c) shows that the increase in resistance value leads to a regular decrease in resonance levels, consistent with the expected damping effect. As the resistance increases, the resonance amplitudes gradually decrease.

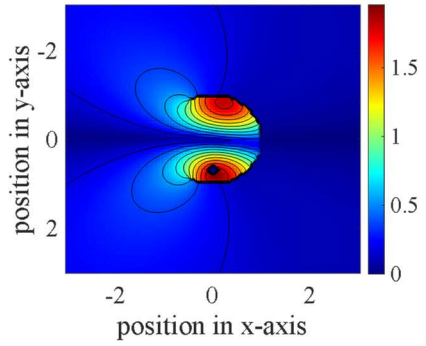

(a)

$(x_0 = 0, y_0 = -0.7, \xi_1 = \xi_2 = 0.1\text{i}, k = 2.23)$

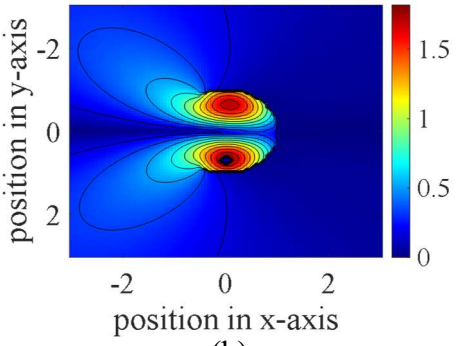

(b)

$(x_0 = 0, y_0 = -0.7, \xi_1 = \xi_2 = 0.3\text{i}, k = 2.86)$

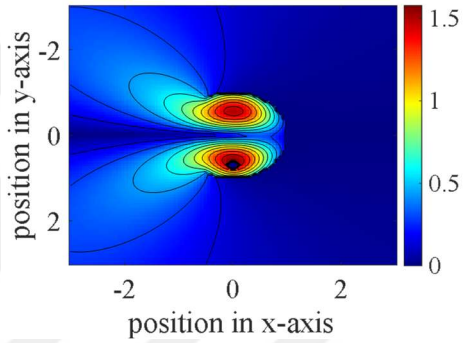

(c)

$(x_0 = 0, y_0 = -0.7, \xi_1 = \xi_2 = 0.5\text{i}, k = 3.198)$

Figure 2.6 : Near H-field amplitudes for different parameters when the source is located inside $\left(\theta = \pi - \frac{\pi}{3}, a = 1\right)$.

In Figure 2.6(a), the parameters ξ_1 and ξ_2 are selected as $0.1i$, and the wave number is determined as $k = 2.23$. Under these conditions, it is observed that there is high energy on the source location and also there is high energy area opposite side of the source location. A shadow is observed on the outer part of the circular arc. Shadow formation is also observed from the center of the circular arc towards the direction of the opening.

In Figure 2.6(b), the values ξ_1 and ξ_2 are increased to $0.3i$, and the wave number is taken as $k = 2.86$. There is high energy point again on the source location also opposite side has another high energy point. Also there is energy outside of the circular strip and this energy amplitute is bigger than Figure 2.6(a). Shadow formation is also similar to Figure 2.6(a), but slightly more.

In Figure 2.6(c), the parameters ξ_1 and ξ_2 were set to $0.5i$ and the wave number k was chosen as 3.198. It has similar formation like Figure 2.6(b). However, energy outside of the circle a bit higher than Figure 2.6(b).

Overall, these results show effect of the parameters ξ_1, ξ_2, and k on the wave amplitude, highlighting how important to determine these parameters for electromagnetic scattering characteristics of the system.

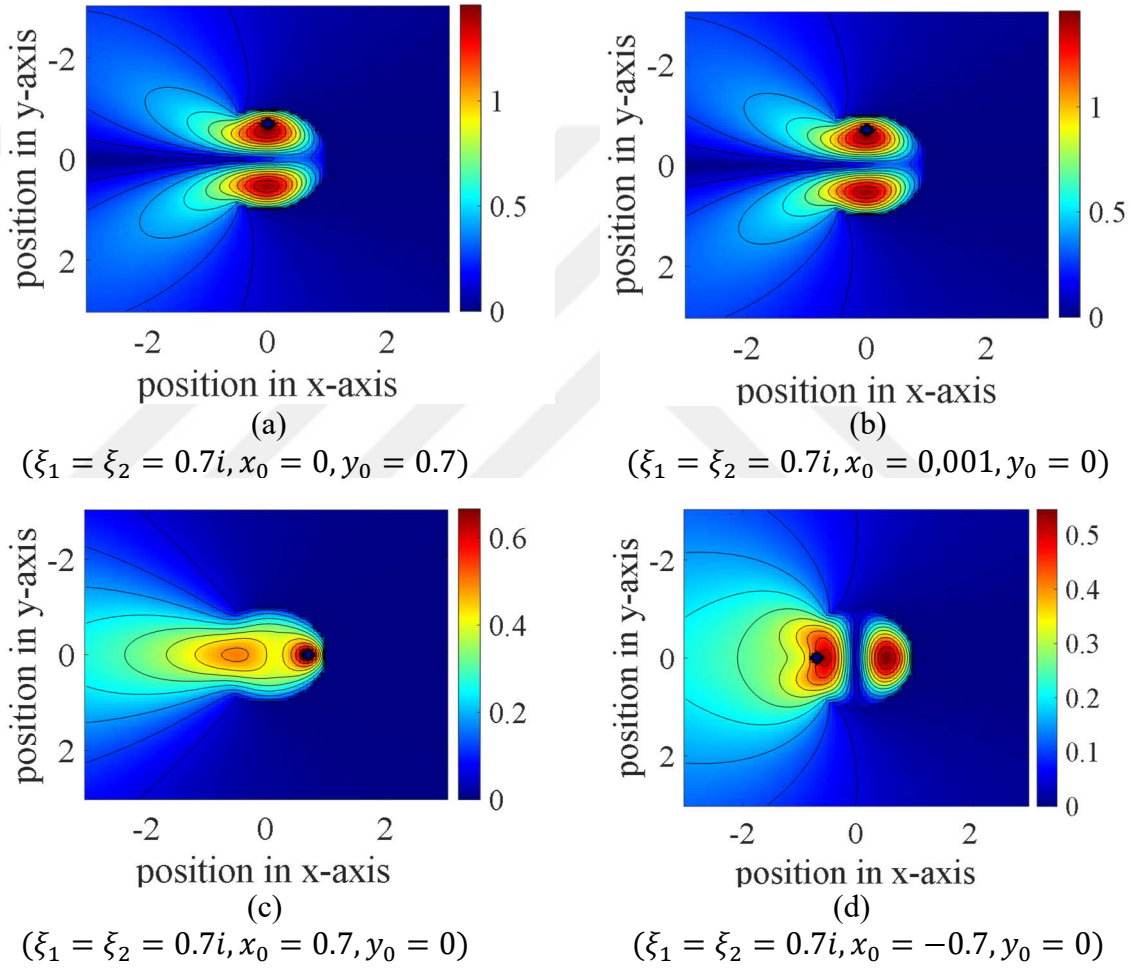

Figure 2.7 : Near H-field amplitudes for different positions of the line source $\left(\theta = \pi - \frac{\pi}{3}, a = 1, k = 3.38\right)$.

In Figure 2.7, observations were made by changing only the source location while keeping all parameters fixed. It is seen that the location of the source plays a decisive role in the overall distribution and amplitude of the H-field in both the inner and outer regions of the circular arc.

Figure 2.7(a) shows a high radiation pattern in the region where the source location is and where the opposite pole is located. As we move outwards from the aperture of the circular arc, the pattern decreases as the wave power decreases, turning into a shadow. Similarly, a shadow is seen on the closed back surface of the circular arc.

In Figure 2.7(b), the source location is centered. A high radiation pattern is seen in the inner part of the circular arc. However, shadow formation is also seen outwards from behind the source. Intense shadow formation is clearly visible on the outer surface of the circular arc.

In Figure 2.7(c), the source location is moved closer to the edge of the inner part of the arc. When the source is located at this position, high energy is only seen above the source, and the radiation pattern is seen spreading outwards from the aperture of the circular arc. As in the other figures, shadow formation is observed behind the circular arc in Figure 2.7(c).

Finally, in Figure 2.7(d), the source location is positioned towards the aperture of the circular arc. The radiation pattern is observed above the source and inside the arc like previous figures. Similarly, the energy flow is seen outwards from the aperture of the circular arc. Shadow formation is observed behind and in the center of the circular arc.

2.2.2 Comparison and convergence

This subsection presents a comparison based on the total radar cross section (TRCS) and its corresponding near-field distributions.

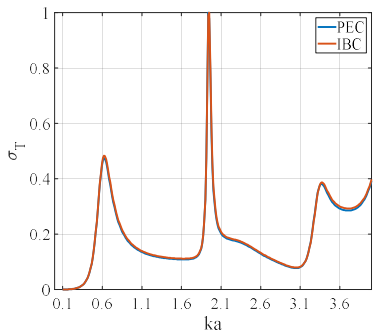

(a)

$(x_0 = -0.5, y_0 = 0.5, \xi_1 = \xi_2 = 0.0001)$

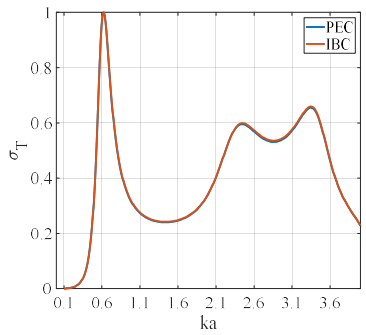

(b)

$(x_0 = 0.5, y_0 = 0, \xi_1 = \xi_2 = 0.0001)$

Figure 2.8 : TRCS comparison with PEC circular strip for $(\theta = \pi - \frac{\pi}{4}, a = 1)$.

The TRCS results obtained in Figure 2.8(a)–(b) are compared with the results presented in the reference study [9] for the perfect electrical conductor (PEC) circular strip, which is considered as the limit state of impedance boundary conditions. The aim of this comparison is to evaluate the accuracy and validity of the method used by comparing it with the reference results and examining the degree of deviation.

The numerical results show that between the method which we are using and the reference study differences is less than 1% in terms of total radar cross section. This level of similarity show that it can remake the PEC limiting case with high level of correctness.

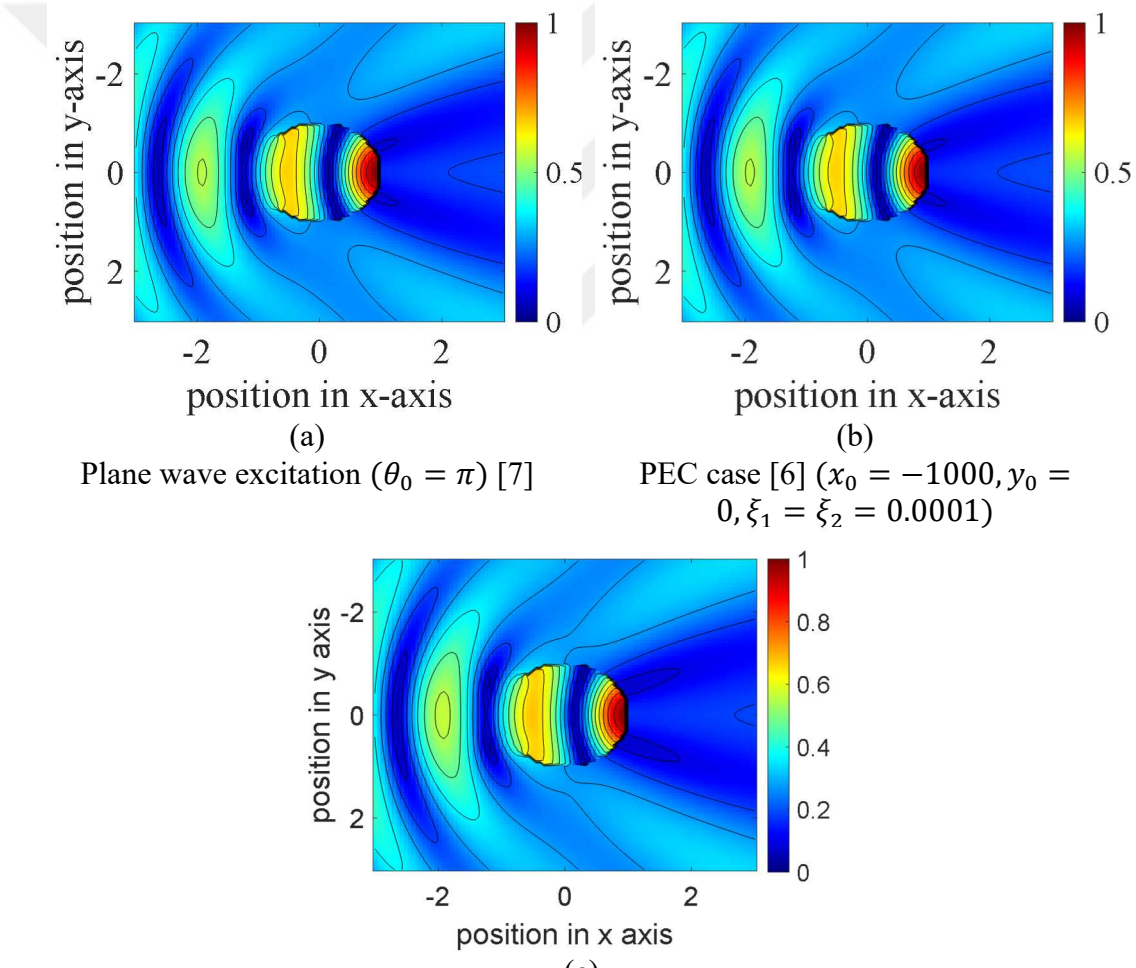

(a)
Plane wave excitation ($\theta_0 = \pi$) [7]

(b)
PEC case [6] ($x_0 = -1000, y_0 = 0, \xi_1 = \xi_2 = 0.0001$)

(c)
Proposed Approach ($\xi_1 = \xi_2 = 0.0001, x_0 = -1000, y_0 = 0$)

Figure 2.9 : The normalized near H-field comparison with the different source excitations for ($\theta = \pi - \frac{\pi}{4}, k = 2.3, a = 1$).

Figure 2.9 shows the normalized near-field H-field distributions obtained plane wave and line source excitations for a circular strip with a PEC surface. The results obtained with the used method are compared with [9,25]. The difference between the used method and reference results is less than 4% for near-field distributions.

These comparisons confirm that the proposed method is almost similar to the results in reference studies. The small observed deviations show that the improved formulation can correctly predict scattering mechanisms and near-field distributions.

In this case, the findings demonstrate that the proposed approach can be reliably used to analyze and characterize the electromagnetic scattering behavior of circular strip structures in terms of both total radar cross-section and near-field distribution.

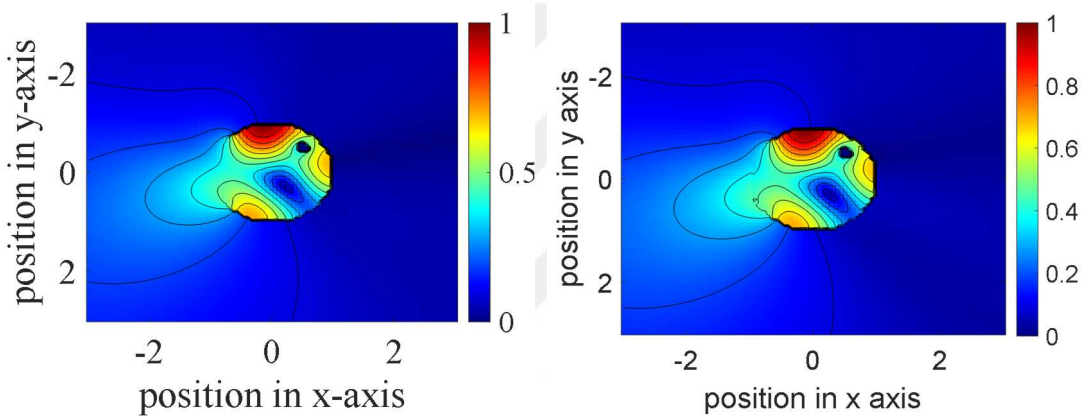

(a) ($x_0 = 0.5, y_0 = -0.5, \xi_1 = \xi_2 = 0.0001$)

(b) PEC case [6] ($x_0 = 0.5, y_0 = -0.5$)

Figure 2.10 : The normalized near H-field comparison for PEC and Impedance Surfaces ($\theta = \pi - \frac{\pi}{4}, k = 2.3, a = 1$).

Figure 2.10 compares the case where the source is positioned within a circular arc with the corresponding PEC(Perfect Elektric Conductor). The purpose of this comparison is to examine the effect of source position on scattering behavior and to show its similarity to the deviation in the PEC condition.

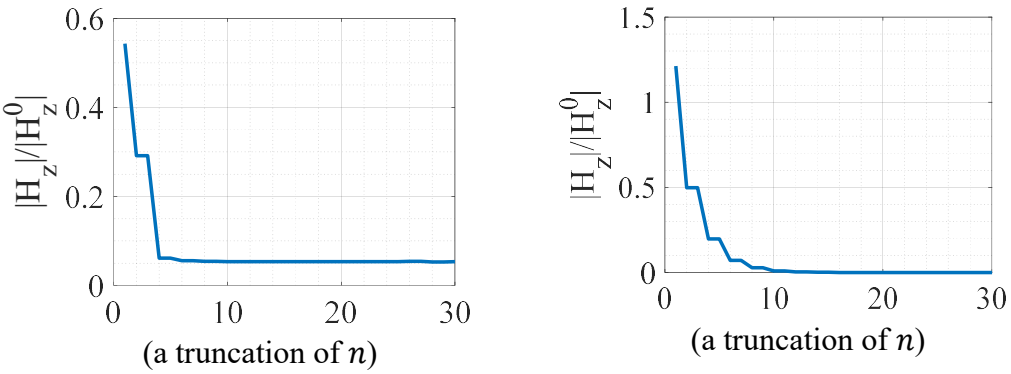

(a)
source is inside
$(x_0 = 0, y_0 = 0, \xi_1 = \xi_2 = 10j, k = 4)$

(b)
source is outside
$(x_0 = 2, y_0 = 0, \xi_1 = \xi_2 = 10j, k = 2)$

Figure 2.11 : Convergence of the boundary conditions for $\left(\theta_0 = \pi - \frac{\pi}{3}, a = 1\right)$.

Figure 2.11 presents a convergence analysis by increasing the number of unknowns in equations (13), (15) by n for cases where the source location is inside and outside the circular arc. This analysis was performed to verify the convergence behavior of the numerical solution and to determine the appropriate truncation level that provides the expected accuracy.

In the case of PMC (Perfect Magnetic Conductor) or near-PMC, the tangential component of the H-field on the surface of the circular arc approaches zero. In this case, the ratio of the total field to the incident tangential component tends towards zero.

The numerical results show that convergence occurs more slowly when the source is located inside the circular arc compared to when the source is outside the strip. This is an expected result due to the complex structure that the presence of the circular strip introduces to the scattering problem. In the case where the source is within the strip, in order to achieve an error level of less than 3%, the truncation number in equations (13) and (15) must be chosen such that $n > 50$.

The analytical-numerical method used in this study exhibits a favorable convergence performance for the approximate solution. For the parameters examined, it was observed that the truncation level $n = ka + 5$ reached the solution with an error below 5%, which shows that the method can obtain reliable results with low computational cost. Overall, Figure 2.11 shows the transition of the numerical solution and provides

insights into the truncation level required for achieving accurate results for different source locations and impedance boundary conditions.

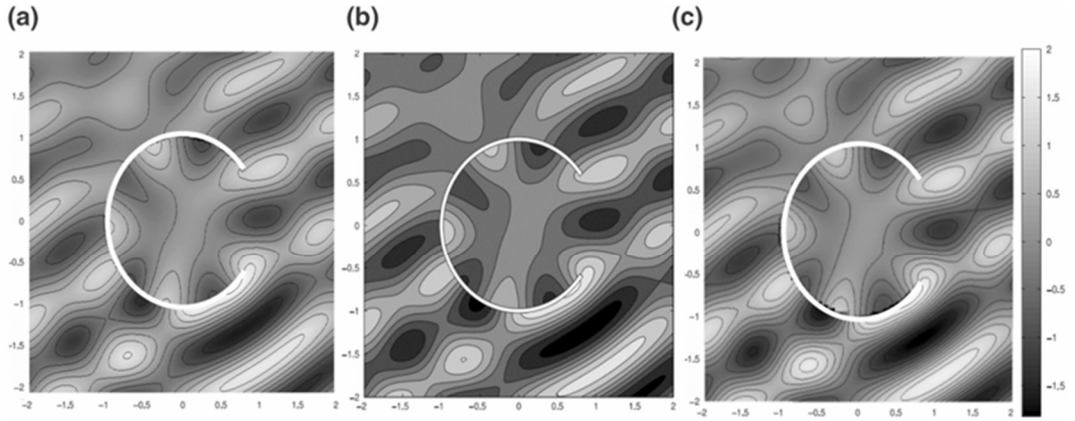

$(ka = 2\pi, \theta = \frac{4\pi}{5}$ and $\theta_0 = \frac{2\pi}{3})$

Figure 2.12: The comparison of the total field H_z distributions with (a) Orthogonal Polynomials Method for perfect electric conducting (PEC) surface [25], (b) embedding formulae method [55], and the proposed method with ($\xi_1 = \xi_2 = 0.001$)

Figure 2.12 presents a comparative analysis of diffraction results obtained from two reference studies and the proposed formulation. Specifically, Figure 2.12(a) examines diffraction from a PEC surface, Figure 2.12(b) shows an alternative comparison technique, and Figure 2.12(c) illustrates the proposed method based on an impedance boundary condition. For H-polarized incidence, selecting very small impedance values ($\xi_1 = \xi_2 = 0.001$) effectively represents the Neumann boundary condition on the total magnetic field. The numerical results indicate that the inconsistency among the three approaches remains below 5%, and the field distributions at the boundaries and edges exhibit consistent behavior even under oblique incidence and high-frequency scenarios. A notable advantage of the proposed approach is its ability to flexibly tune the surface impedance, allowing the realization of various boundary conditions such as Dirichlet, Neumann, and mixed types.

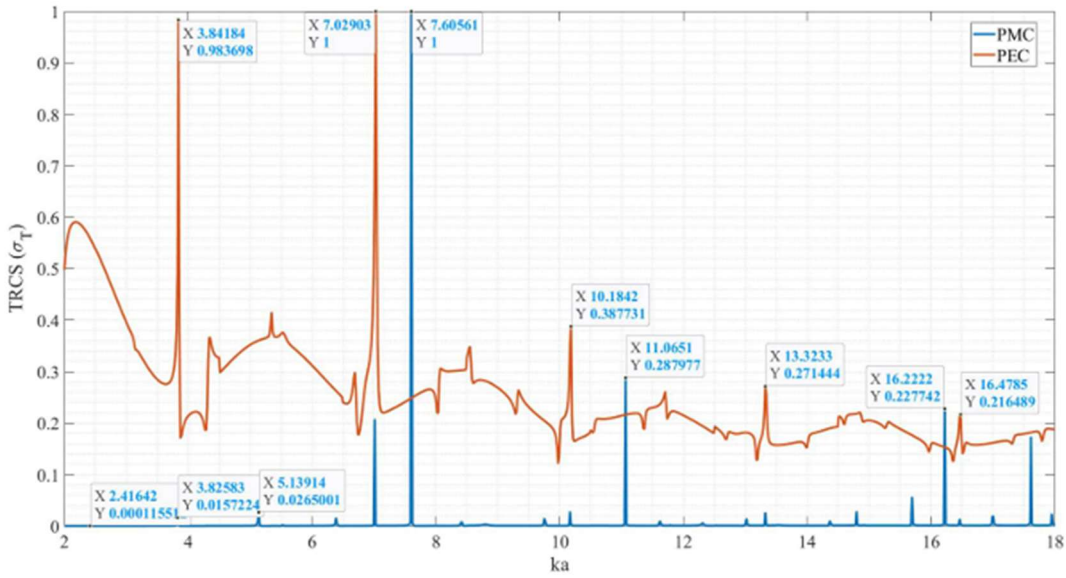

Figure 2.13: The resonance characteristics for small apertures $\theta = \pi - \pi/100$ and $\theta_0 = \pi$

Figure 2.13 demonstrates the validity of the proposed methodology. For a small aperture, resonant behavior is expected to occur at the zeros of the Bessel function and its derivative. As shown, the resonance peaks for PEC and PMC cases align with the zeros of the Bessel function and its derivative, under H-polarized incidence. These results confirm that the impedance boundary condition correctly reproduces PEC and PMC limits.

2.3 Outcomes

This section of the thesis investigates the electromagnetic scattering problem caused by an H-polarized line source interacting with a double-sided circular spring having variable impedance boundary conditions. The aim is to contribute to the design and optimization of electromagnetic devices and systems by analyzing the effect of impedance parameters on the resonance characteristics of the structure.

Accurate modeling of wave behavior in structures defined by specific geometric and boundary conditions is crucial for understanding electromagnetic scattering from circular arcs with impedance boundary conditions. Such analyses show a better

understanding of fundamental electromagnetic mechanisms and form the basis for many engineering applications based on resonance and scattering.

In this context, a method has been developed in which integral equations are solved using an analytical-numerical approach and the unknown surface current densities on the scatterer are expressed by orthogonal polynomial expansions. The total radar cross-section and near-field distributions have been examined in detail in terms of fundamental parameters such as the position of the line source, the internal and external surface impedance values of the scatterer, wavenumber, and aperture size. The obtained results have been systematically compared with studies in the literature to demonstrate the accuracy and effectiveness of the proposed method.

Unlike previous studies, this thesis widely investigates the electromagnetic field behavior under the combined effect of the cylindrical source's position, aperture size, and impedance values. The findings clearly reveal that these parameters play a decisive role in the resonance response and electromagnetic scattering characteristics of the circular strip structure. Based on our findings, resonators with impedance surfaces ofcertain complex values and specific positions of the cylindrical source perform better than the traditional Perfect Electric Conductor (PEC) and Perfect Magnetic Conductor (PMC) resonators in certain resonant scenarios.

3. ELECTROMAGNETIC LINE SOURCE SCATTERING BY THE CIRCULAR ARC WITH FRACTIONAL BOUNDARY CONDITION

3.1 The Formulation of the Problem

This section we trying to explain the problem of electromagnetic scattering from a circular strip with a discrete aperture is mathematically addressed using fractional boundary conditions. Fractional boundary conditions arise as a natural generalization of classical impedance boundary conditions, enabling the modeling of intermediate behaviors between fully conductive surfaces and impedance-controlled surfaces. From a physical perspective, such boundary conditions are used to effectively approximate complex surface behaviors that cannot be adequately represented by classical integer-order models, such as thin coatings, metasurface structures, composite surfaces, or frequency-dependent and nonlocal surface interactions.

The inclusion of fractional boundary conditions in the scattering problem allows for a more flexible and physically meaningful modeling of surface-wave interactions. This approach both bridges the gap between ideal boundary conditions and realistic electromagnetic surfaces and directly contributes to the physical interpretation of the resonance and scattering mechanisms investigated throughout this thesis. Thus, the mathematical formulation presented in this section provides a consistent and connected foundation within the overall structure of electromagnetic scattering.

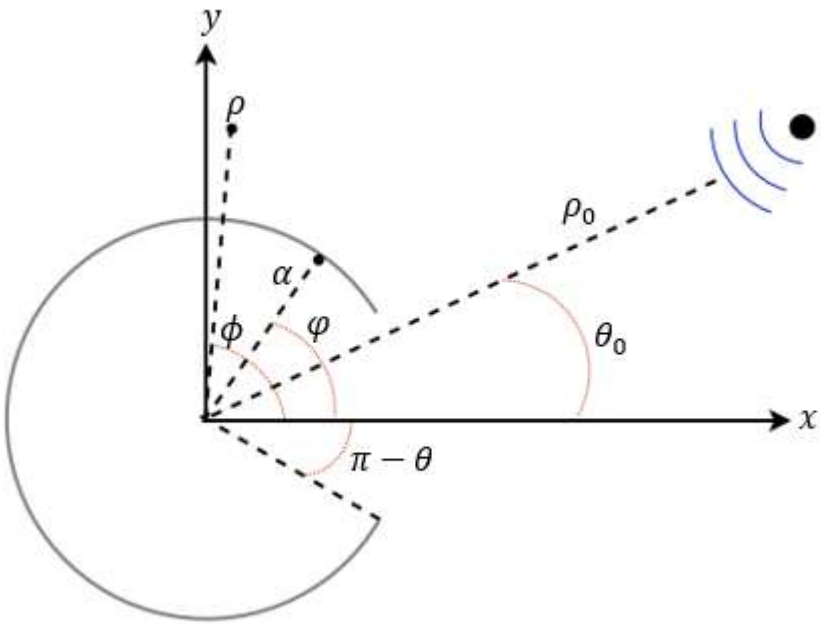

Figure 3.1 : The geometry of the problem-2

Figure 1 is the geometry of our problem-2. The variables ϕ and ρ represent the polar coordinates of the observation point. a and φ represent the polar angular coordinates defined on the surface of the circular arc. Finally, the parameters θ_0 and ρ_0 represent the polar coordinates of the incident source. Similarly like we did in impedance circular arc case:

$$H^s = \int_0^{2\pi} \mu(\varphi) D_{k\rho}^{\alpha} H_0^{(1)}(k|\vec{r} - \vec{r}'|) d\varphi, \rho' = a \tag{3.1}$$

Here instead of regular derivative we have the fractional derivative this come from [4]

The scattered magnetic field, denoted by H^s, is a fundamental quantity in the analysis of electromagnetic scattering problems[27]. In this thesis, the scattered field is expressed by equation (3.1). Here, $H_0^{(1)}$ represents the Hankel function of first-kind and the zero order. The integral is defined in the interval $\varphi \in [0,2\pi]$, covering the entire angular field.

The function $\mu(\varphi)$ describes the magnetic permeability distribution in the scattering region, while ρ and ρ' represent the radial distances measured from the origin; $\rho' = a$ corresponds to the position of the scattering surface.

The use of the addition theorem is shown in equation (3.2). This theorem allows for the rearrangement of field expressions in a way suitable for analysis, and it has been used to eliminate singularities that arise in the integral of this formulation:

$$H_0^{(1)}(k|\vec{r}-\vec{r}'|) = \begin{cases} \sum_{n=-\infty}^{\infty} J_n(k\rho)H_n^{(1)}(k\rho')e^{in(\phi-\varphi)} \rho \leq a \\ \sum_{n=-\infty}^{\infty} J_n(k\rho')H_n^{(1)}(k\rho)e^{in(\phi-\varphi)} \rho \geq a \end{cases} \quad (3.2)$$

The total magnetic field is defined by equation (3.3), which includes the fractional derivative operator $D_{k\rho}^{\alpha}$. This operator represents the fractional derivative of order α defined with respect to the radial variable $k\rho$ and forms the basis of the fractional boundary condition used in this study. The boundary condition applied at the position $\rho = a$ is expressed as follows:

$$D_{k\rho}^{\alpha}(H_z^0 + H_z^s)_{\rho=a} = 0 \quad (3.3)$$

The incident magnetic field at this boundary condition is defined by equation (3.4):

$$H_z^0 = -\frac{i\omega\varepsilon_0 A_0}{4} H_0^{(1)}(k|\rho-\rho_0|) \quad (3.4)$$

where:

$$Z = \frac{i\omega\varepsilon_0 A_0}{4}$$

The parameters, amplitude A_0, angular frequency ω and dielectric permittivity ε_0 of free space in equation (3.4) together describe the physical properties of the incident field.

The fractional derivative of the Hankel function used in the formulation is given in equation (3.5) [26]:

$$D_t^{\alpha}H_n^{(1)}(t) = \frac{(t-a)^{-\alpha}}{\Gamma(1-\alpha)}H_n^{(1)}(t) + \sum_{p=1}^{\infty}\frac{\Gamma(\alpha+1)}{\Gamma(p+1)\Gamma(\alpha-p+1)}\frac{(t-a)^{p-\alpha}}{\Gamma(p-\alpha+1)} \quad (3.5)$$

Fractional calculus involves different, non-equivalent definitions of fractional derivatives; the most commonly used among these are the Riemann–Liouville, Caputo, and Grünwald–Letnikov definitions. The choice of fractional operator directly affects both the mathematical structure and the physical interpretation of the problem.

This thesis used the definition of the Riemann–Liouville fractional derivative. This definition is suitable for boundary value problems encountered in electromagnetic scattering. From a physical perspective, the Riemann–Liouville operator allows for the modeling of surface interactions showing memory effects and spasial dispersion; such effects cannot be efficiently represented by classical integer-order boundary conditions:

$$H_z^0 = -Z \sum_{m=-\infty}^{\infty} \begin{cases} J_m(k\rho) H_m^{(1)}(k\rho_0) e^{im(\phi-\theta_0)} & \rho \le \rho_0 \\ J_m(k\rho_0) H_m^{(1)}(k\rho) e^{im(\phi-\theta_0)} & \rho \ge \rho_0 \end{cases} \tag{3.6}$$

Equation (3.6) is obtained after using the addition theorem. It presents an expression for the incident magnetic field H_z^0. In the region $\rho \le \rho_0$, the field is expressed in terms of the Bessel function J_m evaluated at point $k\rho$ and the first-kind Hankel function $H_m^{(1)}$evaluated at point $k\rho_0$, and the phase factor $e^{im(\phi-\theta_0)}$.

In the case $\rho \ge \rho_0$, the field expression includes the Bessel function J_m evaluated at point $k\rho_0$ and the Hankel function $H_m^{(1)}$ evaluated at point $k\rho$, and the same angular dependence.

$$H^s = \frac{4i}{\varepsilon} \sum_{m=-\infty}^{\infty} \mu_m \begin{cases} J_m(k\rho) D_{k\rho}^{\alpha} H_m^{(1)}(\varepsilon) e^{im\phi} & \rho \le a \\ D_{k\rho}^{\alpha} J_m(\varepsilon) H_n^{(1)}(k\rho) e^{im\phi} & \rho \ge a \end{cases} \tag{3.7}$$

Equation (3.7) shows the expression for the scattered magnetic field H^s, where the singularity in the scattering problem is eliminated by applying the addition theorem. For derivation of this formula we used the same technics as in the case of impedance arc (formulas (2.7)-(2.11)).

The expression separates two different regions with respect to the reference radius a of the radial coordinate ρ. In the case $\rho \le a$, the field is expressed by a combination of Bessel and Hankel functions, while for $\rho \ge a$, the roles of these functions are

reversed. The $\frac{4i}{\varepsilon}$ factor in the field expression ensures that the field is scaled in such a way as to preserve the correct amplitude and phase properties.

Equation (3.8) shows the fractional boundary condition used in this case. In this context, the total magnetic field is obtained by applying the fractional derivative operator to the incident and scattered field components.

$$D_{k\rho}^{\alpha}\left(-Z\sum_{m=-\infty}^{\infty}J_m(k\rho)H_m^{(1)}(k\rho_0)e^{im(\phi-\theta_0)} + \frac{4i}{\varepsilon}\sum_{m=-\infty}^{\infty}\mu_m J_m(k\rho)D_{k\rho}^{\alpha}H_m^{(1)}(\varepsilon)e^{im\phi}\right)_{\rho=a} = 0 \tag{3.8}$$

$$\left(-Z\sum_{m=-\infty}^{\infty}D_{k\rho}^{\alpha}J_m(ka)H_m^{(1)}(k\rho_0)e^{im(\phi-\theta_0)} + \frac{4i}{\varepsilon}\sum_{m=-\infty}^{\infty}\mu_m D_{k\rho}^{\alpha}J_m(ka)D_{k\rho}^{\alpha}H_m^{(1)}(\varepsilon)e^{im\phi}\right)_{\rho=a} = 0 \tag{3.9}$$

$$-Z\sum_{m=-\infty}^{\infty}D_{k\rho}^{\alpha}J_m(ka)H_m^{(1)}(k\rho_0)e^{im(\phi-\theta_0)} + \frac{4i}{\varepsilon}\sum_{m=-\infty}^{\infty}\mu_m D_{k\rho}^{\alpha}J_m(ka)D_{k\rho}^{\alpha}H_m^{(1)}(\varepsilon)e^{im\phi} = 0 \tag{3.10}$$

In equations (3.9) and (3.10), the fractional derivative operation is enclosed in parentheses. This will lead to the left-hand side of the equation being transferred to the right-hand side, followed by the execution of the iterative procedure accordingly.

In equation (3.9), the left side is expressed as a mode sum defined by the index m. Here, $D_{k\rho}^{\alpha}$ represents the fractional derivative evaluated at the point $\rho = a$ and defined with respect to the variable ρ. The resulting terms include the Bessel and Hankel functions evaluated at the points ka and $k\rho_0$, and the angular phase factor $e^{im(\phi-\theta_0)}$.

Equation (3.10) has a similar structure, but it does not have any restrictive conditions on its right side. Therefore, this equation is considered as an independent relation representing the unconstrained equilibrium state of the system.

$$\frac{4i}{\varepsilon}\sum_{m=-\infty}^{\infty}\mu_m D_{k\rho}^{\alpha}J_m(ka)D_{k\rho}^{\alpha}H_m^{(1)}(\varepsilon)e^{im\phi} = Z\sum_{m=-\infty}^{\infty}D_{k\rho}^{\alpha}J_m(ka)H_m^{(1)}(k\rho_0)e^{im(\phi-\theta_0)} \tag{3.11}$$

In this context, the variables ' η ' and ' φ ' are integrated into this equation, resulting in the final version denoted as equation (3.11):

$$\eta = \frac{\varphi}{\theta} \; \varphi = \theta\eta$$

$$\frac{4i}{\varepsilon}\sum_{m=-\infty}^{\infty}\mu_m\gamma_m e^{im\theta\eta} = Z\sum_{m=-\infty}^{\infty}D_{k\rho}^{\alpha}J_m(\varepsilon)H_m^{(1)}(k\rho_0)e^{im(\theta\eta-\theta_0)} \tag{3.12}$$

$$\gamma_m = D_{k\rho}^{\alpha}J_m(\varepsilon)D_{k\rho}^{\alpha}H_m^{(1)}(\varepsilon)$$

In equation 3.12, the term γ_m is introduced, defined as $D_{k\rho}^{\alpha}J_m(\varepsilon)D_{k\rho}^{\alpha}H_m^{(1)}(\varepsilon)$ encapsulating the interplay between 'η' and 'φ' within the formula.

The left-hand side involves a summation over various modes m, incorporating coefficients μ_m and phase factors $e^{im\phi}$. Meanwhile, the right-hand side features a similar summation structure multiplied by the scaling factor Z.

The Gegenbauer polynomials are indicated by the expression $C_n^{\nu+\frac{1}{2}}$. The current density is expressed as equation (3.13):

$$\mu(\eta) = (1-\eta^2)^{\nu}\sum_{n=0}^{\infty}x_n C_n^{\nu+\frac{1}{2}}(\eta) \tag{3.13}$$

Current density is expressed as a summation of the Gegenbauer polynomial because the weighting function of the Gegenbauer polynomial (for this weight function) satisfied an edge condition. In our problem ν equals $\alpha - 0.5$. If ν is 0.5 current vanishes on the edges but if ν is -0.5 it becomes infinite.

According to [9,33], the Fourier coefficient of equation (3.14) is given as follows:

$$\begin{aligned}\hat{\mu}_m &= \frac{\theta}{2\pi}\int_{-1}^{1}\mu(\eta)e^{-im\theta\eta}d\eta \\ &= \frac{\theta}{2\pi}\int_{-1}^{1}\left[(1-\eta^2)^{\nu}\sum_{n=0}^{\infty}x_n C_n^{\nu+\frac{1}{2}}(\eta)\right]e^{-i} \quad d\eta \\ &= \frac{\theta}{2\pi}\sum_{n=0}^{\infty}x_n\int_{-1}^{1}(1-\eta^2)^{\nu}C_n^{\nu+\frac{1}{2}}(\eta)e^{-im\theta}\; d\eta\end{aligned} \tag{3.14}$$

Upon substitution of the requisite equations and subsequent calculation, equation (3.15) emerges as follows:

$$\begin{aligned}\hat{\mu}_m &= \frac{\theta}{2\pi}\sum_{n=0}^{\infty} x_n \int_{-1}^{1}(1-\eta^2)^{\nu} C_n^{\nu+\frac{1}{2}}(\eta)e^{-im\theta\eta}d\eta \\ &= \frac{\theta}{2\pi}\sum_{n=0}^{\infty} x_n \frac{\Gamma(2\nu+1+n)}{\Gamma\left(\nu+\frac{1}{2}\right)}\frac{\pi 2^{\frac{1}{2}-\nu} i^n}{\Gamma(n+1)}(-m\theta)^{-\left(\nu+\frac{1}{2}\right)} J_{\nu+n+\frac{1}{2}}(-m\theta) \\ &= \frac{\theta}{2\Gamma\left(\nu+\frac{1}{2}\right)}\sum_{n=0}^{\infty} i^n x_n \frac{\Gamma(2\nu+1+n)}{\Gamma(n+1)}\frac{2^{\frac{1}{2}-\nu}}{(-m\theta)^{\left(\nu+\frac{1}{2}\right)}} J_{\nu+n+\frac{1}{2}}(-m\theta) \\ &= \frac{\theta}{\Gamma\left(\nu+\frac{1}{2}\right)}\sum_{n=0}^{\infty} i^n x_n \beta_n^{\nu+\frac{1}{2}} \frac{J_{\nu+n+\frac{1}{2}}(-m\theta)}{(-2m\theta)^{\left(\nu+\frac{1}{2}\right)}}\end{aligned} \tag{3.15}$$

$$\beta_n^{\nu+\frac{1}{2}} = \frac{\Gamma(2\nu+1+n)}{\Gamma(n+1)}$$

This equation represents the result after performing the prescribed computations, where $\hat{\mu}_m$ is determined as a function of various parameters and Bessel functions $J_{\nu+n+\frac{1}{2}}(-m\theta)$.

The Fourier transform of our formula in its final form is as follows [34]:

$$\hat{\mu}_m = \frac{\theta}{\Gamma\left(\nu+\frac{1}{2}\right)}\sum_{n=0}^{\infty} i^n x_n \beta_n^{\nu+\frac{1}{2}} \frac{J_{\nu+n+\frac{1}{2}}(-m\theta)}{(-2m\theta)^{\left(\nu+\frac{1}{2}\right)}} \tag{3.16}$$

Also exponent term in (3.12) from [33]:

$$\begin{aligned}e^{im\theta\eta} = \left(\frac{2}{m\theta}\right)^{\nu+\frac{1}{2}}\Gamma\left(+\frac{1}{2}\right)\left\{\sum_{k=0}^{\infty} i^k(-1)^{\frac{k}{2}}\left(k+\nu\right.\right. \\ \left.\left.+\frac{1}{2}\right)J_{k+\nu+\frac{1}{2}}(m\theta)C_k^{\nu+\frac{1}{2}}(\eta)\right\}\end{aligned} \tag{3.17}$$

We then substitute the expression of the Fourier transform (3.16) of the current density and the exponent (3.17) in (3.12), we arrive at the final Linear Algebraic Equation System (LAES) by this approach (3.18):

$$2\pi\theta\sum_{p=0}^{\infty}(-i)^{p}x_{p}\beta_{p}^{\nu+\frac{1}{2}}Q_{pk}^{\nu+\frac{1}{2}}=\mathrm{A}_{k}^{\nu+\frac{1}{2}}$$

$$Q_{pk}^{\nu+\frac{1}{2}}=\sum_{m=-\infty}^{\infty}\gamma_{m}J_{\nu+p+\frac{1}{2}}(m\theta)J(m\theta)\left(\frac{1}{m\theta}\right)^{2\nu+1}$$

$$\mathrm{A}_{k}^{\nu+\frac{1}{2}}=Z\Gamma(\nu+\frac{1}{2})2^{\nu+\frac{1}{2}}\sum_{m=-\infty}^{\infty}D_{k\rho}^{\alpha}J_{m}(\varepsilon)H_{m}^{(1)}(k\rho_{0})e^{-im\theta_{0}}J_{k+\nu+\frac{1}{2}}(m\theta)\left(\frac{1}{m\theta}\right)^{\nu+\frac{1}{2}} \tag{3.18}$$

Again like in case of impedance arc the case where m=0 should be considered seperately:

$$\mathrm{A}_{k}^{\nu+\frac{1}{2}}(k=0)=J_{0}'(\varepsilon)\left(\frac{1}{\Gamma(\nu+\frac{3}{2})}\left(\frac{1}{2}\right)^{\nu+\frac{1}{2}}\right) \tag{3.19}$$

3.2 Numerical Results and the Comparison

This section presents and compares the numerical results obtained to investigate the effect of fractional boundary conditions on the overall scattering behavior of the circular arc. The analysis is performed on the Total Radar Cross Section (TRCS) for different fractional order values α, in parallel with the approach used in [26]. TRCS is a quantitative measure of the total electromagnetic energy scattered by the structure and is used as a fundamental parameter in evaluating the resonance behavior.

An increase in the TRCS value shows that the structure interacts more strongly with the incident electromagnetic field and that the resonance modes are excited more effectively. Conversely, a decrease in TRCS indicates that impedance effects or scattering response are weakened and resonance is suppressed. In this context, by

examining the changes in TRCS, it is possible to observe which parameter combinations strengthen or weaken the resonance behavior.

This section analyzes the effects of the position of the line source (inside or outside the circular arc), wave number, aperture size, and impedance values assigned to the inner and outer surfaces of the fractional circular arc on the TRCS. The aim here is to identify cases that offer more advantageous scattering characteristics compared to classical PEC and PMC cases, and to reveal the potential of fractional boundary conditions in the modeling and design of electromagnetic structures

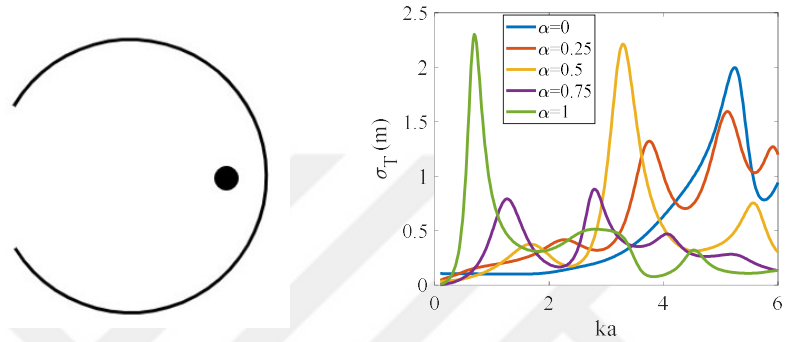

(a) (b)

Figure 3.2: Source location is $x = 0.7,\ y = 0$ and aperture size is $\theta = \pi - \frac{\pi}{3}$, observation points $\alpha = 0.0001,\ 0.25,\ 0.5,\ 0.75,\ 1.$

Figure 3.2(a) shows estimated source locationd and Figure 3.2(b) illustrates the Total Radar Cross Section (TRCS) for a location inside the arc. At this location, the first resonance has a higher frequency under Perfect Magnetic Conductor (PMC) conditions. Conversely, the second resonance at $\alpha = 0.5$ also exhibits a higher frequency. This material performs better than both Perfect Electric Conductor (PEC) and PMC when the source is located at this position.

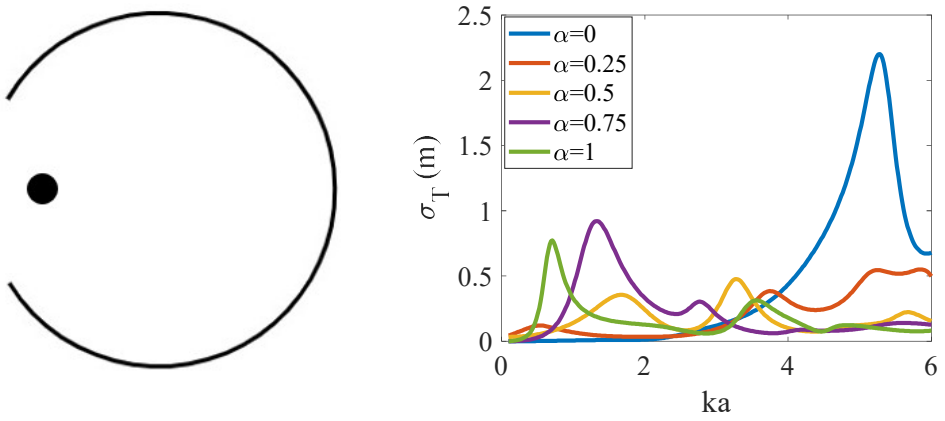

(a) (b)

Figure 3.3: Source location is $x = -0.7,\ y = 0$ and aperture size is $\theta = \pi - \frac{\pi}{3}$, observation points $\alpha = 0.0001,\ 0.25,\ 0.5,\ 0.75,\ 1$.

Figure 3.3(a) is the estimated source location. Figure 3.3(b) illustrates that $\alpha = 0.75$ has a higher frequency at the first resonance. Again this material shows better result than PEC and PMC cases. On the other hand, the second resonance shows a higher frequency value for PEC.

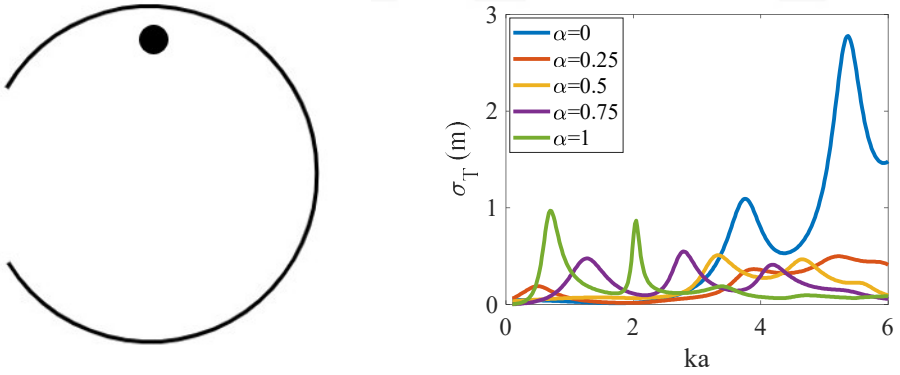

(a) (b)

Figure 3.4: Source location is $x = 0,\ y = 0.7$ and aperture size is $\theta = \pi - \frac{\pi}{3}$, observation points $\alpha = 0.0001,\ 0.25,\ 0.5,\ 0.75,\ 1$.

Figure 3.4(a) exhibit estimated source location and Figure 3.4(b) shows that the higher values are observed for PMC and PEC. Again, this is not what we are looking for in our study.

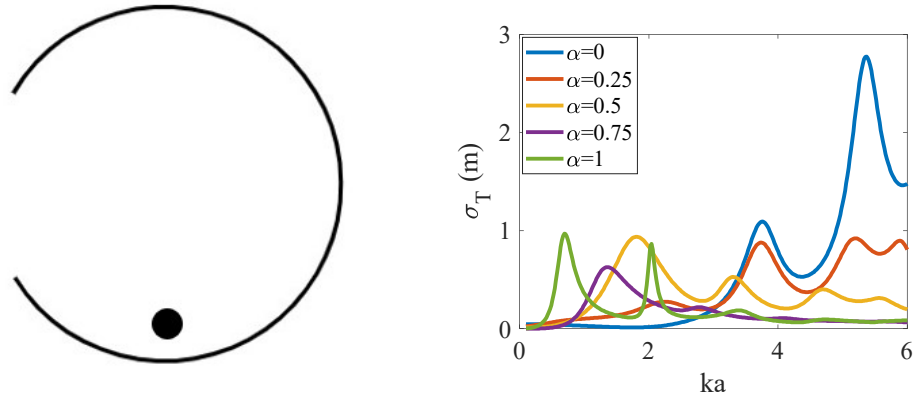

(a) (b)

Figure 3.5: Source location is $x = 0,\ y = -0.7$ and aperture size is $\theta = \pi - \frac{\pi}{3}$, observation points $\alpha = 0.0001,\ 0.25,\ 0.5,\ 0.75,\ 1$.

Figure 3.5(a) presents the source location. Figure 3.5(b) illustrates that the first resonance has higher resonance peak at PMC case, but $\alpha = 0.5$ case is also very close to the PMC case. At the second resonance PEC case has higher resonance peak. Both first and second resonance peaks are the PMC and PEC cases this is again not we are desire to see it.

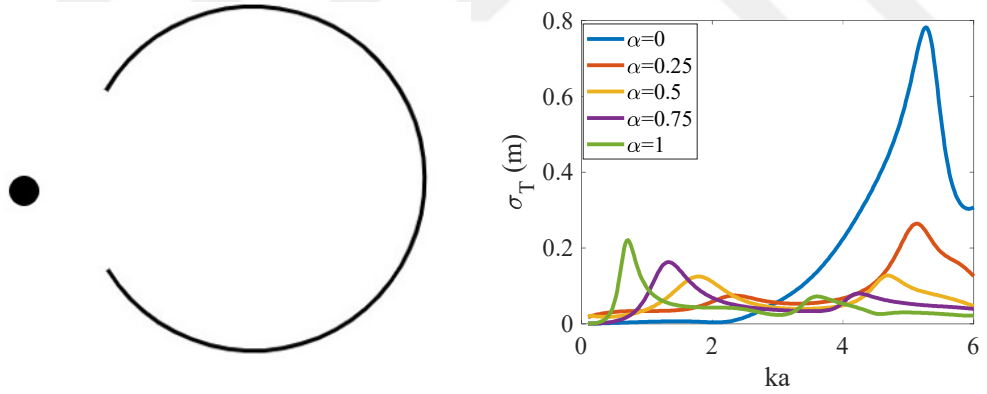

(a) (b)

Figure 3.6: Source location is $x = -1.5,\ y = 0$ and aperture size is $\theta = \pi - \frac{\pi}{3}$, observation points $\alpha = 0.0001,\ 0.25,\ 0.5,\ 0.75,\ 1$.

Figure 3.6(a) shows the estimated source location. Figure 3.6(b) displays the TRCS for a source located outside the arc. At the first resonance, PMC again exhibits a higher frequency, while at the second resonance, PEC shows a higher frequency, as clearly observed.

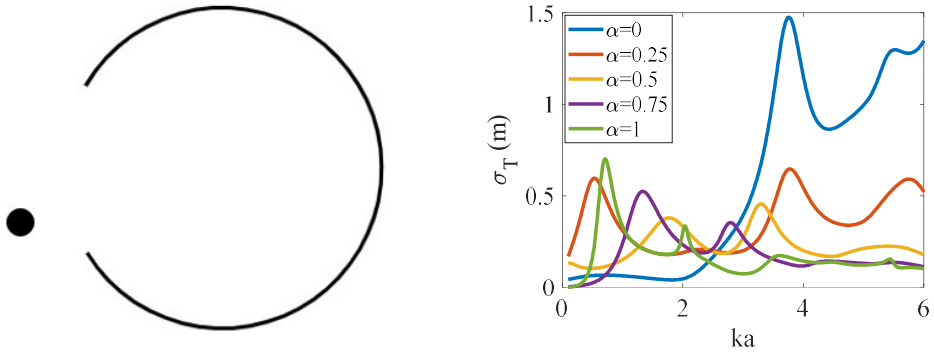

(a) (b)

Figure 3.7: Source location is $x = -1.5,\ y = -1.3$ and aperture size is $\theta = \pi - \frac{\pi}{3}$, observation points $\alpha = 0.0001,\ 0.25,\ 0.5,\ 0.75,\ 1$.

Figure 3.7(a) describe estimated source location. Figure 3.7(b) shows that at the first resonance, PMC is again dominant, although α=0.25 is very close. However, at the second resonance, PEC clearly has a higher frequency.

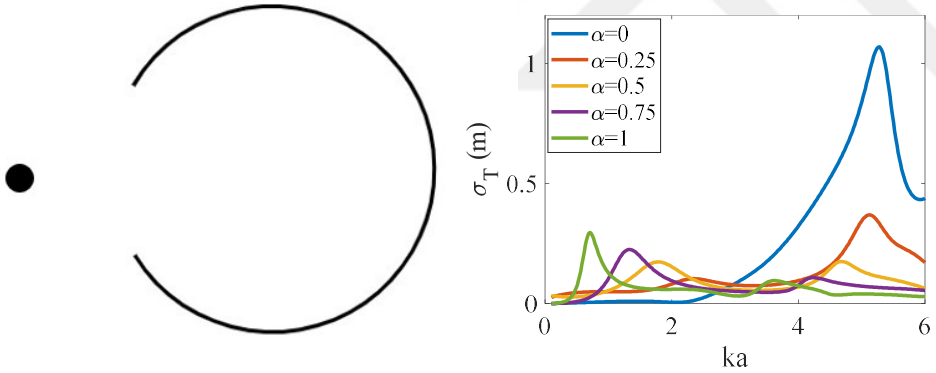

(a) (b)

Figure 3.8: Source location is $x = -1.7,\ y = 0$ and aperture size is $\theta = \pi - \frac{\pi}{3}$, observation points $\alpha = 0.0001,\ 0.25,\ 0.5,\ 0.75, 1$.

Figure 3.8(a) shows the estimated source location. Figure 3.8(b) illustrates that, once again, the first resonance shows PMC with a higher frequency, while the second resonance shows PEC with a higher frequency.

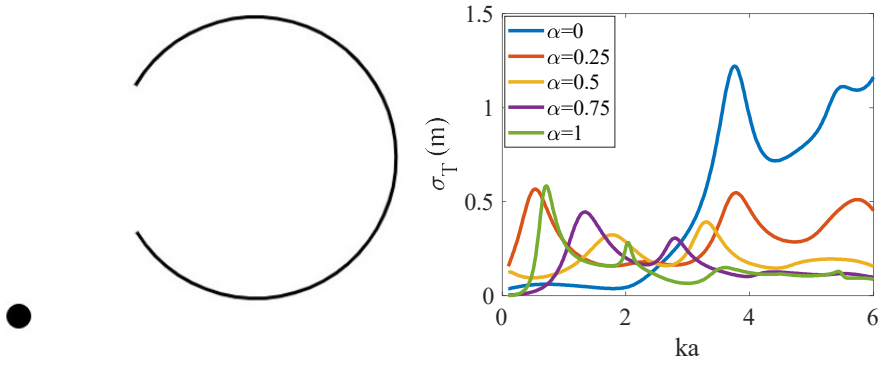

(a) (b)

Figure 3.9: Source location is $x = -1.7,\ y = -1.5$ and aperture size is $\theta = \pi - \frac{\pi}{3}$, observation points $\alpha = 0.0001,\ 0.25,\ 0.5,\ 0.75,\ 1.$

Figure 3.9(a) exhibits source location and Figure 3.9(b) shows that PMC has a higher value at the first resonance, although α=0.25 is very close. At the second resonance PEC has a higher value.

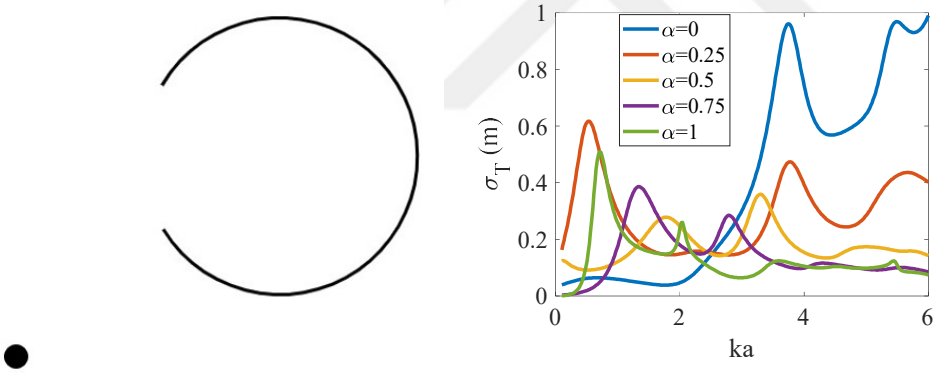

(a) (b)

Figure 3.10: Source location is $x = -1.7,\ y = -1.7$ and aperture size is $\theta = \pi - \frac{\pi}{3}$, observation points $\alpha = 0.0001,\ 0.25,\ 0.5,\ 0.75,\ 1.$

Figure 3.10(a) shows estimated source location. Figure 3.10(b) illustrates that at the first resonance, α=0.25 is higher than the PMC value at this source location. This result is more favorable for our study.

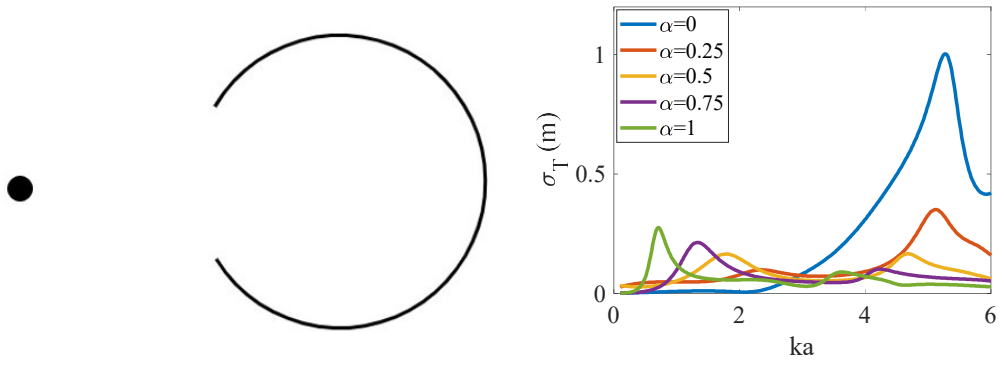

(a) (b)

Figure 3.11: Source location is $x = -1.8,\ y = 0$ and aperture size is $\theta = \pi - \frac{\pi}{3}$, observation points $\alpha = 0.0001,\ 0.25,\ 0.5,\ 0.75,\ 1.$

Figure 3.11(a) shows that the estimated source location. Figure 3.11(b) illustrates that the results for the first and second resonances are again not favorable for our study. Shifting the source along the x-axis alone is not sufficient to achieve good results. Therefore, we attempted to shift the source not only along the x-axis but also along the y-axis to obtain better outcomes.

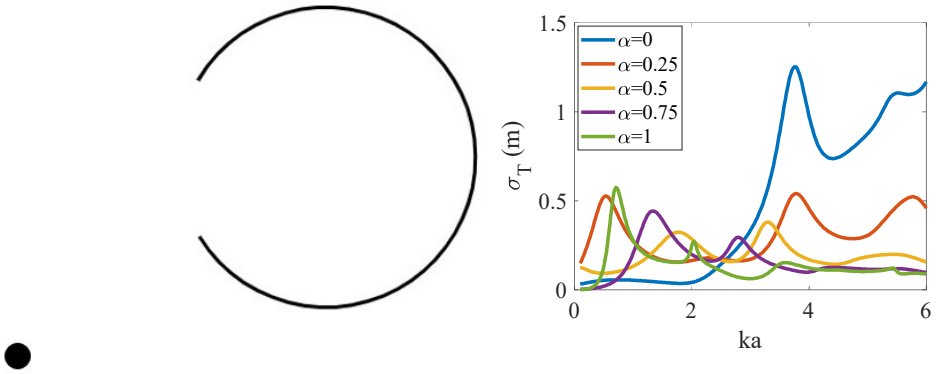

(a) (b)

Figure 3.12: Source location is $x = -1.8,\ y = -1.5$ and aperture size is $\theta = \pi - \frac{\pi}{3}$, observation points $\alpha = 0.0001,\ 0.25,\ 0.5,\ 0.75,\ 1$

Figure 3.12(a) exhibits estimated source location. Figure 3.12(b) shows that the first and second resonances do not yield good results for our study. However, when we attempt to shift along both axes, we can see that the source is very close to the desired location in Figure 3.12.

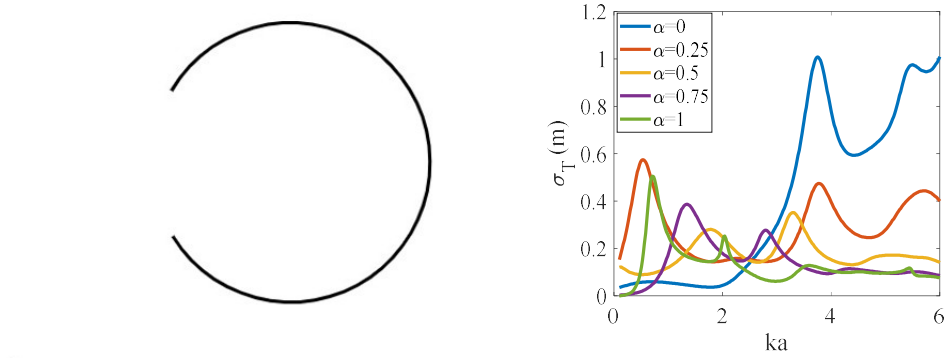

(a) (b)

Figure 3.13: Source location is $x = -1.8,\ y = -1.7$ and aperture size is $\theta = \pi - \frac{\pi}{3}$, observation points $\alpha = 0.0001,\ 0.25,\ 0.5,\ 0.75,\ 1$.

Figure 3.13(a) illustrates estimated source location. Figure 3.13(b) shows that at the first resonance, α=0.25 has a higher frequency, indicating that α=0.25 is better than PMC at this source location.

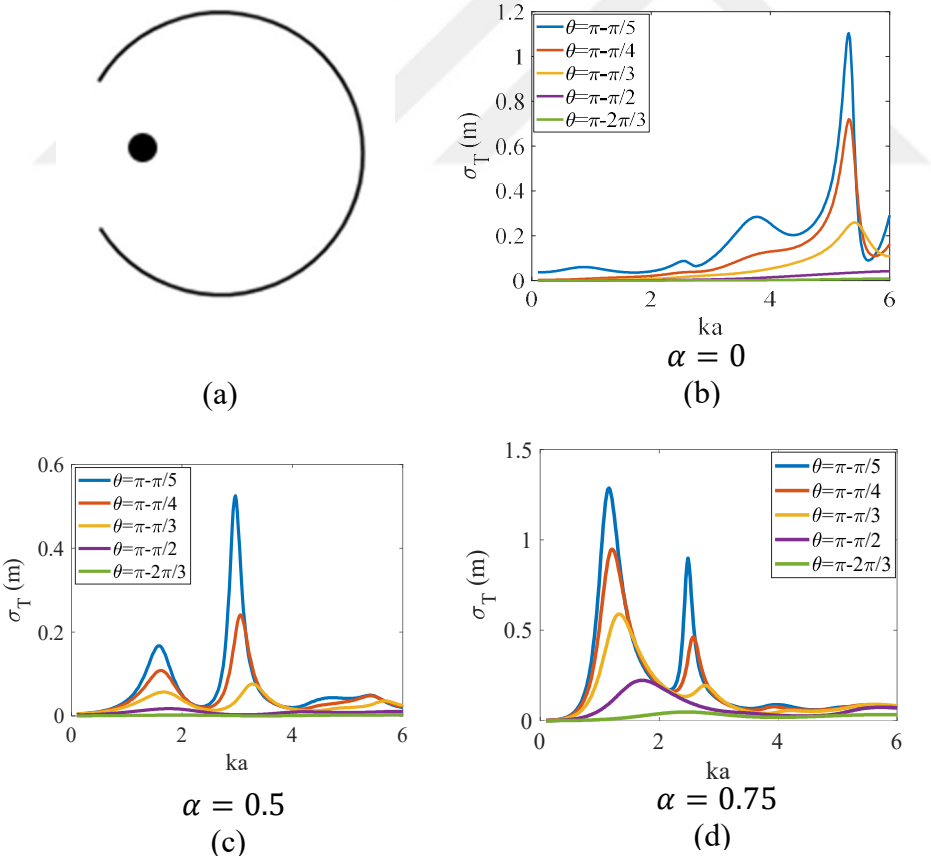

(a) $\alpha = 0$ (b)

$\alpha = 0.5$ (c) $\alpha = 0.75$ (d)

Figure 3.14: Source location is $x = -0.7, y = 0,$ and different aperture sizes $\theta = \pi - \pi/5\,, \pi - \pi/4\,, \pi - \pi/3\,, \pi - \pi/2\,, \pi - 2\pi/3.$

In Figure 3.14, the position of the source remains constant, while the aperture width is modified to analyze its influence on the resonant peaks. Figure 3.14(a) presents the estimated source location with respect to the circular arc configuration. When the aperture angle is α = 0, as shown in Figure 3.14(b), the first and second resonance peaks corresponding to θ = π − π/5 appear considerably stronger than those at other angles. In contrast, when the aperture expands to α = 0.5 in Figure 3.14(c), the second resonance peak shifts, θ = π − π/5 still has the higher value. As illustrated in Figure 3.14(d), for α = 0.75, both first and second resonance peaks θ = π − π/5 slightly have better results than the other resonance peaks.

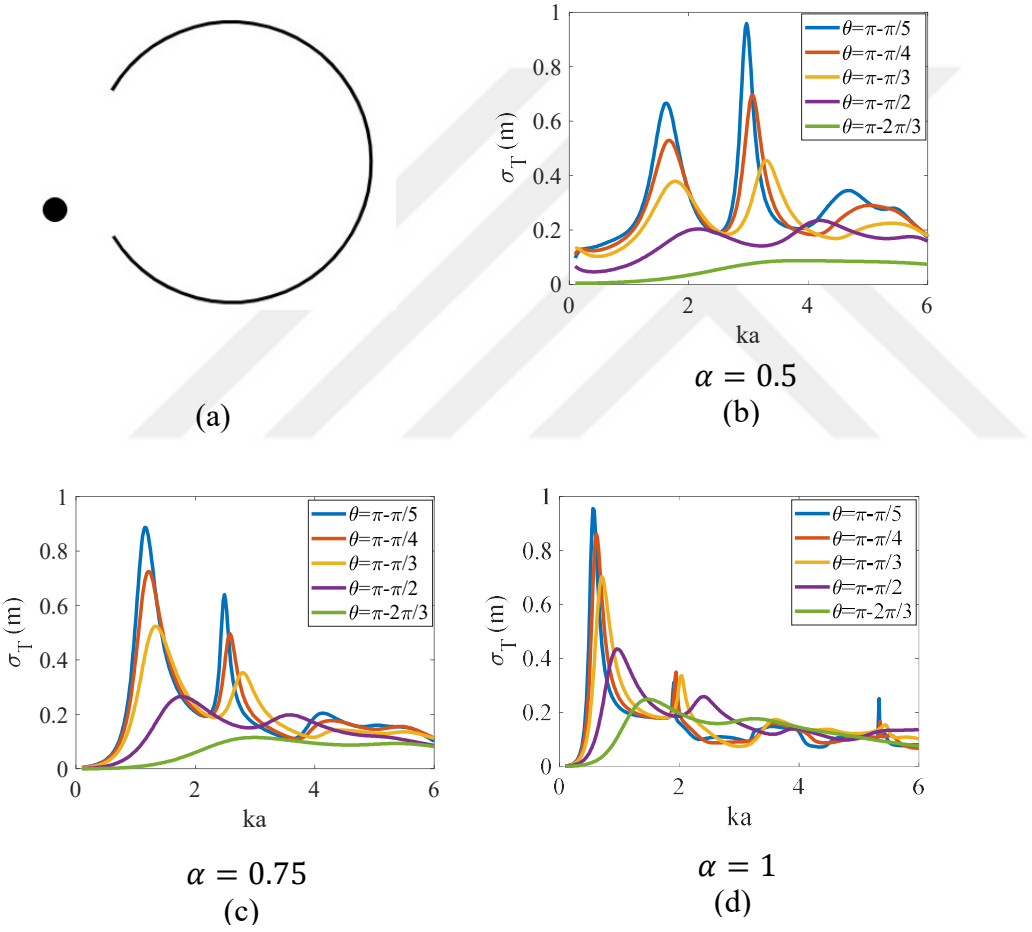

Figure 3.15: Source location is $x = -1.5, y = -1.3$, and different aperture sizes $\theta = \pi - \pi/5, \pi - \pi/4, \pi - \pi/3, \pi - \pi/2, \pi - 2\pi/3.$

In Figure 3.15, the source is located at x = −1.5, y = −1.3, and the effect of changing the aperture size on the resonance characteristics is examined. Figure 3.15(a) shows the spatial relation between the circular arc and the fixed source position. In Figure 3.15(b), for α = 0.5, the first and second resonance peaks at θ = π − π/5 are clearly

dominant, with much higher amplitudes than at other observation angles. Figure 3.15(c), when we increase the aperture size α = 0.75 , again first and second resonance peaks are θ = π − π/5. Finally, in Figure 3.15(d), where α = 1, θ = π − π/4 case is very close to the higher amplitute which is θ = π − π/5. However still θ = π − π/5 has the higher amplitute and this is normally what we expected.

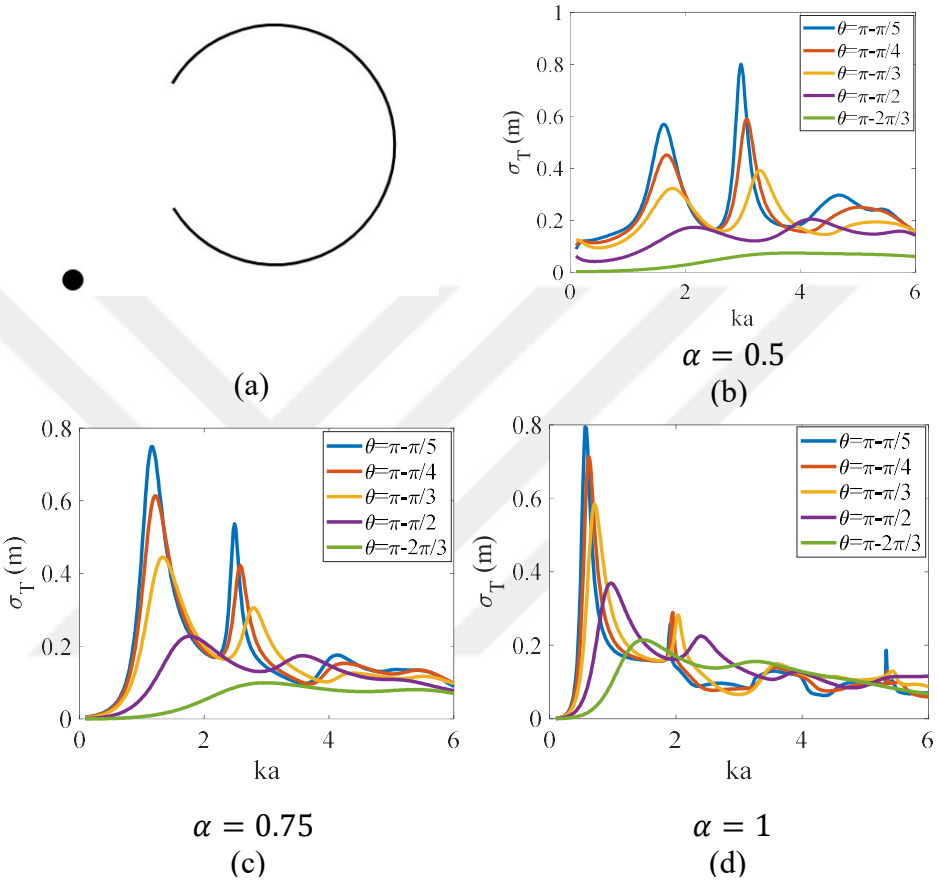

Figure 3.16: Source location is $x = -1.7, y = -1.5$, and different aperture sizes $\theta = \pi - \pi/5, \pi - \pi/4, \pi - \pi/3, \pi - \pi/2, \pi - 2\pi/3.$

In Figure 3.16, the source is positioned at x = −1.7, y = −1.5, and the effect of varying the aperture size on the resonant response is examined. Figure 3.16(a) shows the source location on the circular arc. In Figure 3.16(b), for an aperture size α = 0.5, the resonance peaks are same for both first and second resonances which is θ = π − π/5. The responses for θ = π − π/4 and θ = π − π/3 also have very high amplitudes, but still not higher than the θ = π − π/5. When we increase the aperture size to α = 0.75 in Figure 3.16(c), the resonance peaks for θ = π − π/5 is sharp, and its still the highest resonance for first and second resonance peaks. Finally, in Figure 3.16(d), where α =

1, the resonance pattern becomes more uniform. Again first resonance peak still θ = π − π/5 dominance.

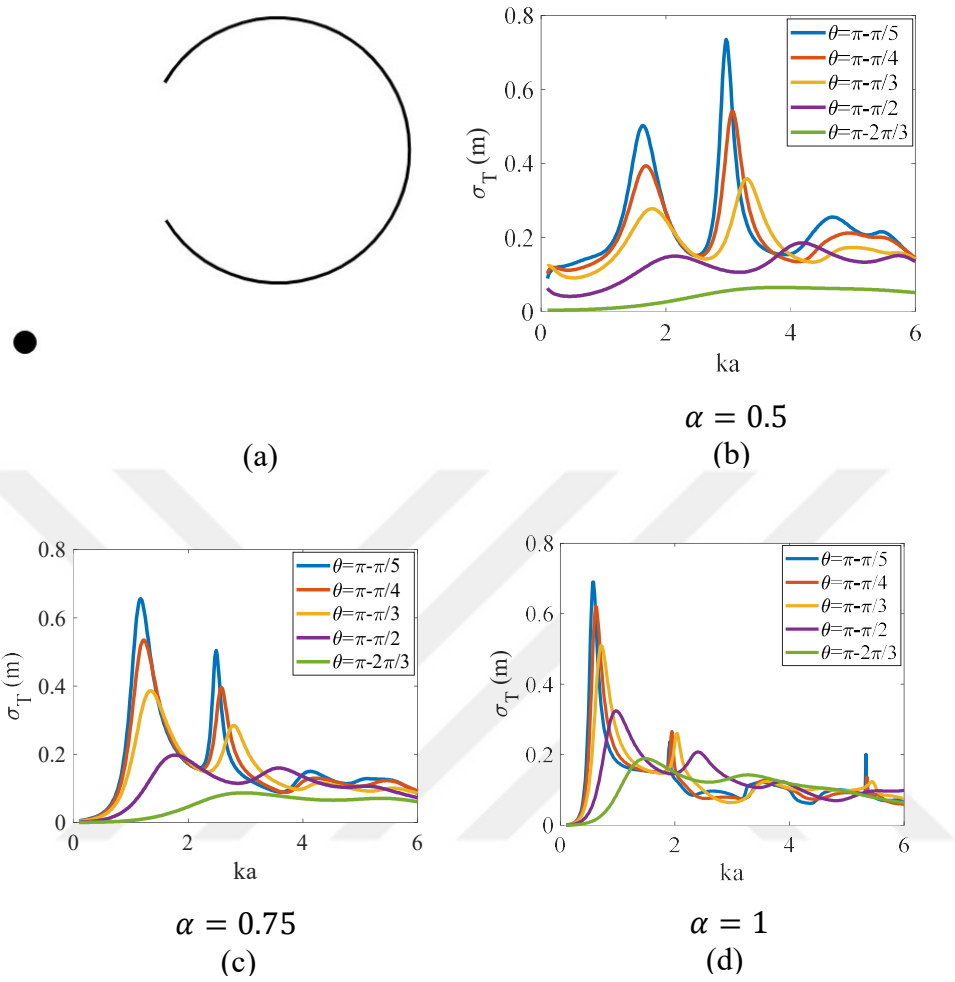

(a)

$\alpha = 0.5$
(b)

$\alpha = 0.75$
(c)

$\alpha = 1$
(d)

Figure 3.17: Source location is $x = -1.7, y = -1.7$, and different aperture sizes $\theta = \pi - \pi/5, \pi - \pi/4, \pi - \pi/3, \pi - \pi/2, \pi - 2\pi/3$.

In Figure 3.17, the source is positioned at x = −1.7, y = −1.7, and the effect of varying the aperture size on the resonant characteristics is analyzed. Figure 3.17(a) illustrates the source location on the circular arc. In Figure 3.17(b), for α = 0.5, the most noticiable resonance peaks at θ = π − π/5 for both the first and second resonances. Figure 3.17(c), the aperture increases to α = 0.75 t still θ = π − π/5 has the highes amplitute, but second resonance peak amplitute lower than the α = 0.5 case. However, θ = π − π/5 is highest resonance peak. Finally, in Figure 3.17(d), where the aperture is α = 1, when we check the first resonance peak still θ = π − π/5 has the highest resonance peak. However, this time θ = π − π/4 is very close to the highest resonance peak. This result again shows that increasing the aperture size reduces scattering effects and results in a more homogeneous distribution of the scattered area.

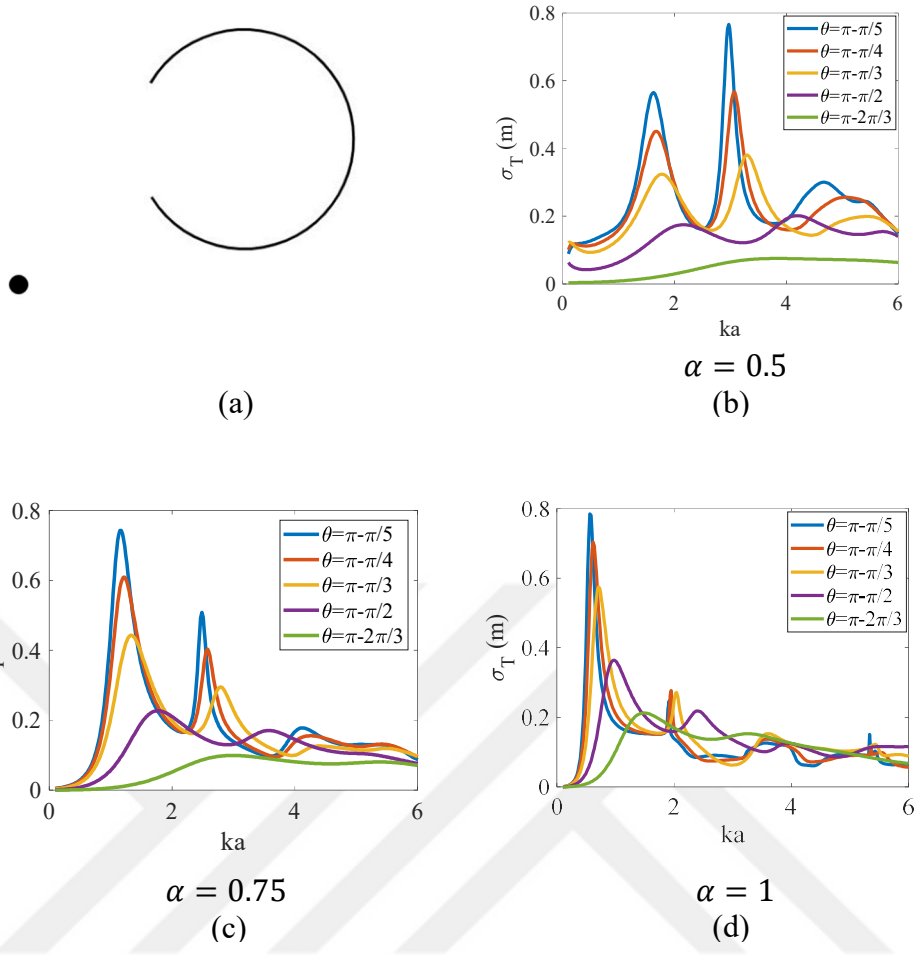

Figure 3.18: Source location is $x = -1.8, y = -1.5$, and different aperture sizes $\theta = \pi - \pi/5, \pi - \pi/4, \pi - \pi/3, \pi - \pi/2, \pi - 2\pi/3$.

In Figure 3.18, the source is located at x = −1.8, y = −1.5, and the influence of changing the aperture size on the resonance behavior is investigated. Figure 3.18(a) shows the source location on the circular arc. In Figure 3.18(b), for α = 0.5, the highest resonance response is observed at θ = π − π/5, where both the first and second peaks are higher than the other resonances. As illustrated in Figure 3.18(c), when the aperture increases to α = 0.75, this pattern remains consistent; θ = π − π/5 continues to exhibit the dominant peaks, while θ = π − π/4 and θ = π − π/3 also maintain relatively elevated values. Finally, in Figure 3.18(d), where α = 1, the resonance becomes smoother across all observation angles, although the first peak at θ = π − π/5 is still slightly higher than the others.

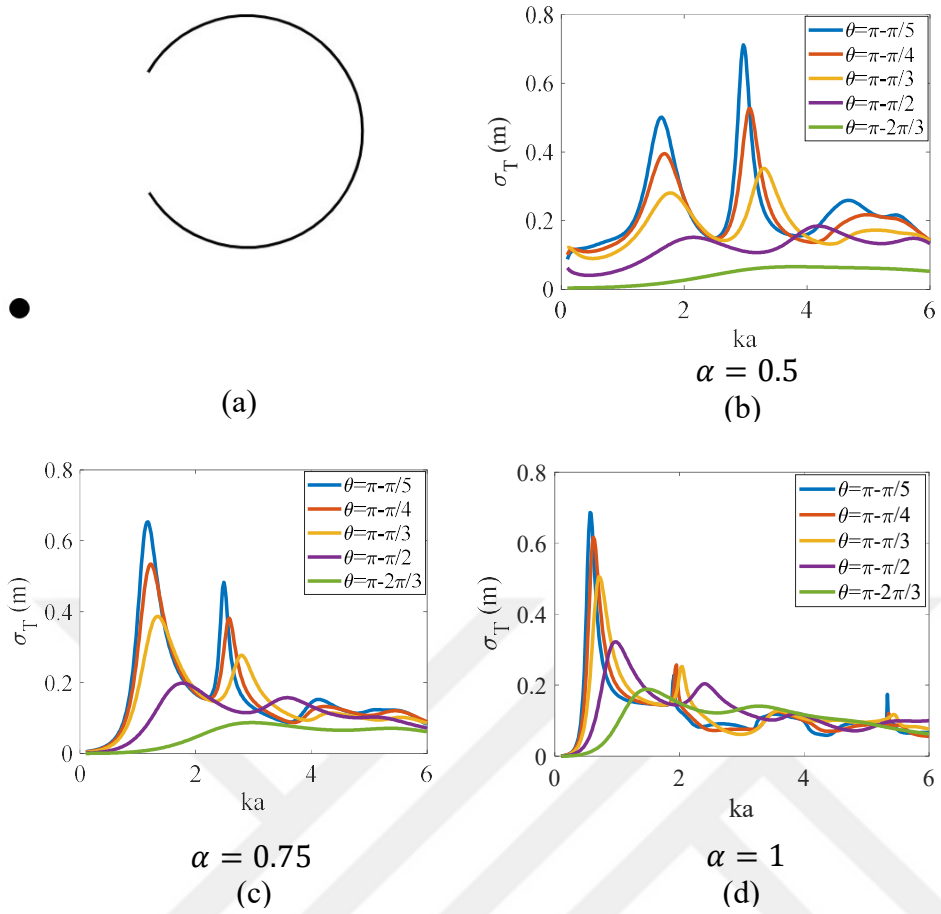

Figure 3.19: Source location is $x = -1.8, y = -1.7$, and different aperture sizes $\theta = \pi - \pi/5, \pi - \pi/4, \pi - \pi/3, \pi - \pi/2, \pi - 2\pi/3$.

In Figure 3.19, the source is positioned at x = −1.8, y = −1.7, and the influence of aperture variation on resonance behavior is examined. Figure 3.19(a) presents the source location on the circular arc. In Figure 3.19(b), for α = 0.5, the resonance pattern is still show the amplitute θ = π − π/5 highest resonance peak. Observation angles such as θ = π − π/4 and θ = π − π/3 also contribute but with slightly lower peak magnitudes. When aperture size increases to α = 0.75 in Figure 3.19(c), this remains consistent; θ = π − π/5 continues to dominant both resonance peaks, while the other angles has minimal variation. Finally, in Figure 3.19(d) given for the case α=1, it is observed that the resonance peaks are broadened and their prominence is reduced. Although θ=π−π/5 still has higher values, the overall scattering response has a more homogeneous structure. This proves that increasing the aperture size smooths the angular resonance variations.

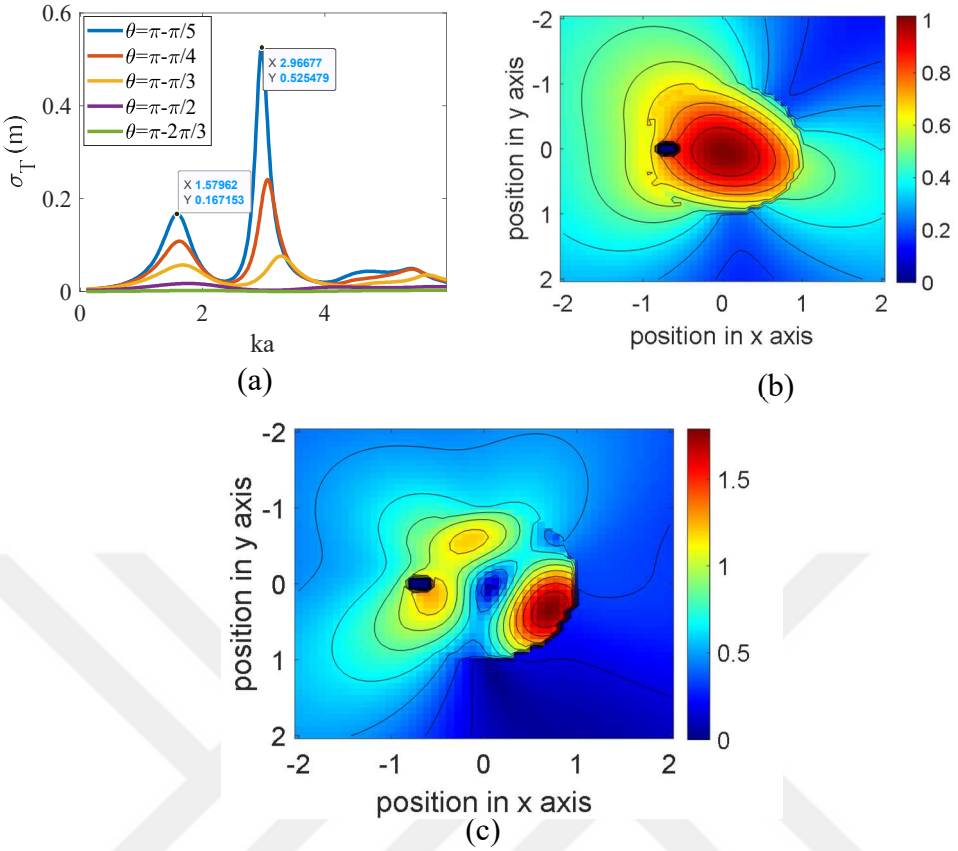

Figure 3.20: Source location is $x = -0.7,\ y = 0,$ for (b) constant is $kk = 1{,}57962$ and aperture size is $\theta = \pi - \pi/5$, for (c) constant is $kk = 2{,}96677$ and aperture size is $\theta = \pi - \pi/5$.

Figure 3.20(a) presents the resonance peaks corresponding to different aperture sizes. Figure 3.20(b) shows the field distribution at the first resonance. In this case, it is observed that the electromagnetic energy is largely concentrated in the inner region of the arc. The energy gradually decreases towards the outer edge of the circular arc. Shadow formations are observed in places on the closed back surface of the circular arc.

The field distribution of the second resonance peak is shown in Figure 3.20(c). The highest energy formation is in the inner part of the circular arc. There is a energy on the source location but this energy formation is smaller then the inner part of the circular arc. Shadow formation is observed to be greater than the shadow formation rate in the field distribution of the first peak.

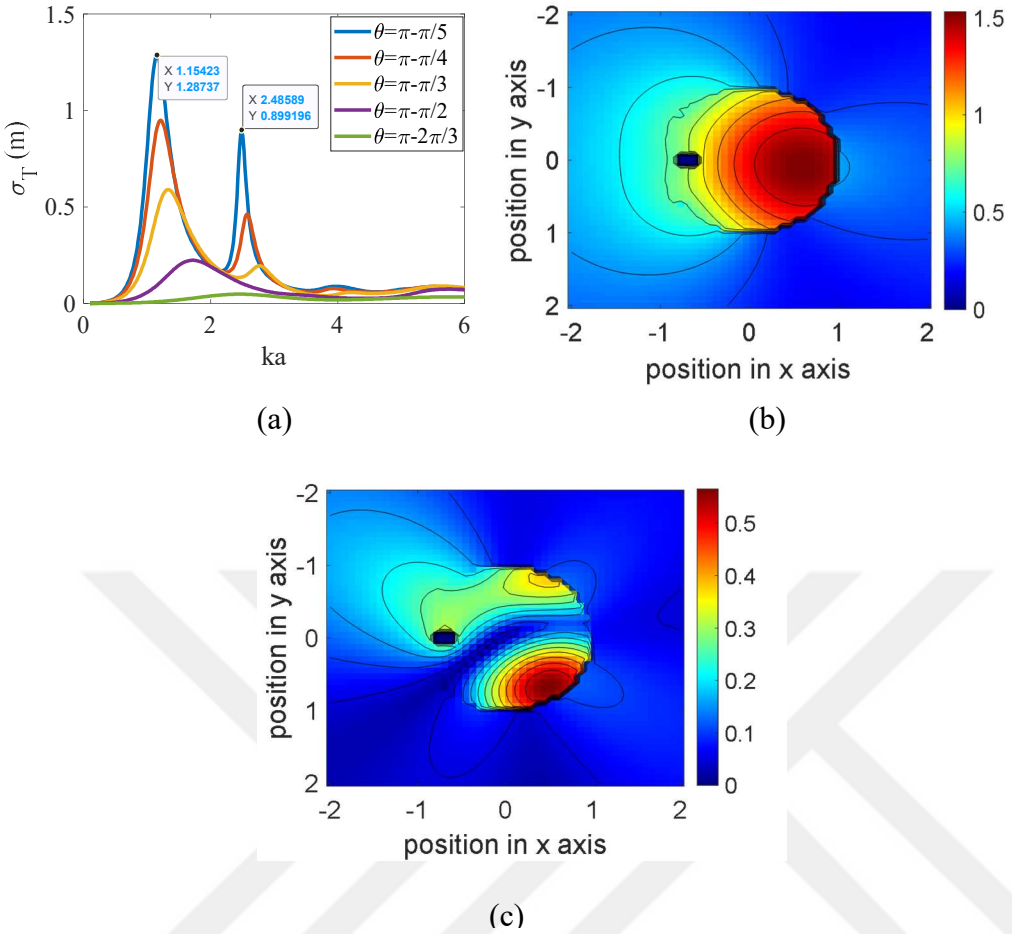

Figure 3.21: Source location is $x = -0.7$, $y = 0$, for (b) constant is $kk = 1{,}15423$ and aperture size is $\theta = \pi - \pi/5$, for (c) constant is $kk = 2{,}48589$ and aperture size is $\theta = \pi - \pi/5$.

Figure 3.21(a) displays the resonance peaks corresponding to various aperture sizes. Figure 3.21(b) shows the field distribution at the second resonance peak. High energy is observed largly concantrated inside of the circular arc. Shadow formation is observed in outside of the circular arc. Figure 3.21(c) shows the third resonance peak. The energy generated on the source point is lower than at the other energy points. The energy density is observed inside of the circular arc but in bottom side. Shadow formation is also observed in the closed area remaining outside the circular arc and center of the circular arc.

3.3 Outcomes

In this section, the electromagnetic diffraction problem of a line source on a circular arc under fractional boundary conditions is solved. Systematic changes in the electromagnetic response within the arc are observed by changing the fractional order

from α=0, representing a perfect electric conductor (PEC), to α=1, representing a perfect magnetic conductor (PMC). This continuous transition clearly reveals boundary behaviors between the classical Dirichlet and Neumann boundary conditions.

The results show that the resonance characteristics of a fractional circular arc are mostly dependent on the position of the line source. Positioning the source inside or outside the arc shows different scattering responses, revealing that the resonance behavior is strongly dependent on the source placement. In the analysis process, fractional derivatives of the Bessel and Hankel functions were obtained and used in the formulation [20]. The use of the fractional derivative representation of the Hankel function is advantageous in increasing computational efficiency.

This thesis is the first study to address the application of fractional boundary conditions to a circular arc geometry excited by a line source.

4. CONCLUSION AND RECOMMENDATIONS

This thesis examines electromagnetic scattering from circular arc configurations excited by a line source within an analytical numerical framework incorporating fractional boundary conditions. The primary goal is to assess whether fractional-order boundary formulations can describe surface interactions in a more adaptable and physically consistent manner than classical integer order conditions. By doing so, the proposed approach establishes a continuous transition between idealized boundary behavior and impedance-based surface models.

The induced surface current densities on the scatterer, along with the associated field distributions, are represented through orthogonal polynomial expansions. Chebyshev and Gegenbauer polynomials are used to correctly satisfy the continuity requirements and edge conditions imposed by the circular geometry. The resulting analytical–numerical formulation demonstrates favorable convergence characteristics and enables the treatment of double-sided impedance configurations within a unified framework.

The influence of key parameters including the fractional order, differences in surface impedance, aperture size, and the position of the line source on scattering behavior has been examined. Numerical findings indicate that fractional boundary conditions play a important role in shaping resonance characteristics, the total radar cross section (TRCS), and near-field distributions. In particular, variations in the fractional order give rise to resonance shifts and field localization patterns that cannot be anticipated using classical integer-order models. Moreover, contrasts between the inner and outer surface impedances are shown to have a decisive impact on the overall scattering response.

The method used was validated through comparisons with analytical results. In the literature for limit cases representing perfect electrical conductor and perfect magnetic conductor boundary conditions. The obtained agreement and limited numerical

deviations prove the correctness of the improved formulation. The ability to achieve high accuracy with low computational cost demonstrates that the method is also usable in engineering applications.

Taken as a whole, the findings of this thesis show that fractional boundary conditions create a practical and effective modeling framework for electromagnetic scattering problems. By extending the classical boundary value formulation, the proposed approach introduces additional flexibility in the representation of surface interactions. The resulting methodology establishes a solid basis for the analysis and design of systems in which surface impedance is a governing factor, including resonant cavities, antenna configurations, radar elements, and electromagnetic absorbing structures.

Furthermore, this framework offers a suitable starting point for future studies involving more complex geometries, different polarization states, and time-dependent fractional operators.

REFERENCES

Sefer, A., and Yapar, A. (2022). Inverse scattering by perfectly electric conducting (PEC) rough surfaces: An equivalent model with line sources. *IEEE Transactions on Geoscience and Remote Sensing*.

Alkumru, A., Dikmen, F., and Doğan, M. (2017). Line source diffraction by perfectly conducting successive steps. *Wave Motion, 68, 253–271.*

Gibson, W. C. (2021). *The method of moments in electromagnetics*. Chapman and Hall/CRC.

Veliev, E. I. (1993). Numerical-analytical approach for the solution to the wave scattering by polygonal cylinders and flat strip structures. In *Analytical and Numerical Methods in Electromagnetic Wave Theory* (Vol. 10). Science House.

Umul, Y. Z. (2019). Wave diffraction by a perfect electromagnetic conductor wedge. *Optik, 182, 761–765.*

Cosan, A. A., Erden, F., and Tretyakov, O. A. (2017). Time-domain energetic properties of the TM-modes in a lossy waveguide. *In 2017 25th Signal Processing and Communications Applications Conference (SIU)*, 1–3.

Senior, T. B. A., and Volakis, J. L. (1995). *Approximate boundary conditions in electromagnetics* (No. 41). IET.

Idemen, M., and Serbest, A. H. (1987). Boundary conditions of the electromagnetic field. *Electronics Letters*,*13*, 704–705.

Karaçuha, K. (2021). General approach to the line source electromagnetic scattering by a circular strip: Both E- and H-polarisation cases. *IET Microwaves, Antennas & Propagation*, *15*, 1721–1734.

Chew, W. C., Hidayetoglu, M., Kudeki, E., and Oelze, M. (2022). Fast numerical integration techniques for 2.5-dimensional inverse problems. *arXiv preprint* arXiv:2207.05915.

Koshovy, G. I. (2017). Mathematical models of acoustic wave scattering by impedance strip. In *2017 XXII International Seminar/Workshop on Direct and Inverse Problems of Electromagnetic and Acoustic Wave Theory (DIPED)*, 71–74.

Chiu, C. C., Sun, C. H., Sun, Y., and Zhang, X. (2010). Time-domain electromagnetic imaging of a two-dimensional metallic cylinder in slab medium using asynchronous particle swarm optimization. In *IMCIC 2010 – International Multi-Conference on Complexity, Informatics and Cybernetics Proceedings*, 195–197.

Apaydin, G., and Ufimtsev, P. Y. (2020). Bistatic scattering at soft–hard strips and

plates: Method of moments (MoM), theory of edge diffraction (TED), and physical theory of diffraction (PTD) analysis. *IET Microwaves, Antennas & Propagation*, *14*, 1117–1123.

Idemen, M. (2000). Confluent edge conditions for the electromagnetic wave at the edge of a wedge bounded by material sheets. *Wave Motion*, *32*, 37–55.

Sefer, A., and Yapar, A. (2021). A spectral domain integral equation technique for rough surface scattering problems. *Waves in Random and Complex Media*, *31*, 1523–1539.

Abrahams, I. D., Assier, R. C., & Nethercote, M. A. (2020). Analytical methods for perfect wedge diffraction: a review. *Wave Motion*, *93*, 102479.

Lindell, I. V., and Sihvola, A. (2019). *Boundary conditions in electromagnetics*. John Wiley & Sons.

Ahmedov, T., Ivakhnychenko, M., and Veliev, E. (2011). Fractional operators approach and fractional boundary conditions. *Electromagnetic Waves*, 117.

Vavilov, V. N., and Veliev, E. I. (1993). Electromagnetic wave diffraction by cylindrical bodies with edges. *Electromagnetics*, *13*, 339–357.

Nosich, A. I., Okuno, Y., and Shiraishi, T. (1996). Scattering and absorption of E- and H-polarized plane waves by a circularly curved resistive strip. *Radio Science*, *31*, 1733–1742.

Dukhopelnykov, S. V., Sauleau, R., and Nosich, A. I. (2020). Integral equation analysis of terahertz backscattering from circular dielectric rod with partial graphene cover. *IEEE Journal of Quantum Electronics*, *56*, 1–8.

Mikhailikova, I., and Dukhopelnykov, S. V. (2022). 2-D scattering and absorption of E-polarized plane wave by a circular dielectric wire with partial graphene cover. In *2022 52nd European Microwave Conference (EuMC)*, 290–293.

Dukhopelnykov, S. V., Nosich, A. I., and Sauleau, R. (2020). Circular dielectric rod with conformal strip of graphene as tunable terahertz antenna: Interplay of inverse electromagnetic jet, whispering gallery and plasmon effects. *IEEE Journal of Selected Topics in Quantum Electronics*, *27*, 1–8.

Dikmen, F., Sever, E., Suvorova, O. A., and Tuchkin, Y. A. (2016). An analytical formulation with ill-conditioned numerical scheme and its remedy: Scattering by two circular impedance cylinders. *Turkish Journal of Electrical Engineering & Computer Sciences*, *24*, 1194–1207.

Karaçuha, K., Tabatadze, V., and Veliyev, E. I. (2022). Electromagnetic plane wave diffraction by a cylindrical arc with edges: H-polarized case. *International Journal of Applied Electromagnetics and Mechanics*, *68*, 13–27. https://doi.org/10.3233/JAE-210018

Alperen, Ö. F., Karaçuha, K., Tabatadze, V., et al. (2022). Electromagnetic diffraction by a slotted cylinder with the fractional boundary condition. *Progress In Electromagnetics Research C*, *128*, 61–71.

Alperen, Ö. F., Karaçuha, K., Tabatadze, V., and Veliev, E. (2022). A new approach in electromagnetic plane wave diffraction by two concentric slotted cylinders with variably placed slits: E and H polarized cases. **IET Microwaves, Antennas & Propagation**. https://doi.org/10.1049/mia2.12252

Karaçuha, E., Karaçuha, K., Tabatadze, V., Veliyev, E., and Zaridze, R. (2022). A fundamental approach: E-polarized electromagnetic wave diffraction by two-dimensional arbitrary-shaped objects with impedance boundary condition. **Journal of Electrical Engineering**, **73**, 426–431.

Balanis, C. A. (1999). *Advanced engineering electromagnetics*. John Wiley & Sons.

Alperen, Ö. F., Karaçuha, K., Tabatadze, V., and Veliev, E. (2022). H-polarized plane wave diffraction by a slotted cylinder with different surface impedances: Solution by the analytical–numerical approach. *IET Microwaves, Antennas & Propagation*.

Meixner, J. (1972). The behavior of electromagnetic fields at edges. *IEEE Transactions on Antennas and Propagation*, *20*, 442–446.

Ishimaru, A. (2017). *Electromagnetic wave propagation, radiation, and scattering: From fundamentals to applications*. John Wiley & Sons.

Brychkov, Iu. A., Marichev, O. I., Prudnikov, A. P., et al. (1990). *Integrals and series (Vol. 2)*.

Brychkov, I. A., Marichev, O. I., and Prudnikov, A. P. (1986). *Integrals and series: Special functions*. CRC Press.

Idemen, M. (2000). Confluent edge conditions for the electromagnetic wave at the edge of a wedge bounded by material sheets. *Wave Motion*, *32*, 37–55.

Uslu, I. E., Yasar, H., Yildiz, G., et al. (2022). Antenna excitation optimization with deep learning for microwave breast cancer hyperthermia. *Sensors*, *22*, 6343.

Beren, J. (1983). Diffraction of an H-polarized electromagnetic wave by a circular cylinder with an infinite axial slot. *IEEE Transactions on Antennas and Propagation*, *31*, 419–425.

Vinogradova, E. (2017). Electromagnetic plane wave scattering by arbitrary two-dimensional cavities: Rigorous approach. *Wave Motion*, *70*, 47–64.

Kobayashi, K., and Nagasaka, T. (2021). Plane wave diffraction by a semi-infinite plate with fractional boundary conditions. *URSI Radio Science Letters*, *3*, 21–42.

Abgaryan, G. V., and Shestopalov, Y. V. (2023). TE-polarized electromagnetic wave diffraction by a circular slotted cylinder. *Mathematics*, *11*, 1991.

Erden, F., and Tretyakov, O. A. (2014). Analytical approach for studying a time-domain cavity problem. In *2014 IEEE Antennas and Propagation Society International Symposium (APSURSI)*, 131–132. IEEE.

Abgaryan, G. V., and Pleshchinskii, N. B. (2019). On the eigen frequencies of rectangular resonator with a hole in the wall. *Lobachevskii Journal of Mathematics*, *40*, 1631–1639.

Smith, P. D., and Vinogradova, E. D. (2022). Q factor enhancement of open 2D resonators by optimal placement of a thin metallic rod in front of the longitudinal slot. *Mathematics*, *10*, 2774.

Dukhopelnykov, S. V., Svezhentsev, A. Y., Volski, V., et al. (2021). Microsized graphene Helmholtz resonator on circular dielectric rod: A tunable sub-THz frequency-selective scatterer. *IEEE Transactions on Antennas and Propagation*, *70*, 2105–2113.

Kobayashi, K., and Nagasaka, T. (2019). Wiener-Hopf analysis of the diffraction by a strip with fractional boundary conditions. In *2019 Photonics & Electromagnetics Research Symposium–Fall (PIERS-Fall)*, 66–72. IEEE.

Koshovy, G. I. (2005). Surface currents induced by an E-polarized wave on curvilinear strips. *Telecommunication and Radio Engineering*, *64*.

Canot, H., and Frénod, E. (2017). Modeling electromagnetism in and near composite material using two-scale behavior of the time-harmonic Maxwell equations. *AIMS Mathematics*.

Ren, S., Wang, Z., and Zhang, Y. (2022). An efficient spectral-Galerkin method for a new Steklov eigenvalue problem in inverse scattering. *AIMS Mathematics*, *7*, 7528–7551.

Kang, S., and Park, W.-K. (2023). A novel study on the bifocusing method for imaging unknown objects in two-dimensional inverse scattering problem. *AIMS Mathematics*, *8*, 27080–27112.

Engheta, N. (1999). Phase and amplitude of fractional-order intermediate wave. *Microwave and Optical Technology Letters*, *21*, 338–343.

Ikiz, T., Kobayashi, K., Koshikawa, S., et al. (2001). Solution of the plane wave diffraction problem by an impedance strip using a numerical-analytical method: E-polarized case. *Journal of Electromagnetic Waves and Applications*, *15*, 315–340.

Ahmedov, T. M., Ivakhnychenko, M. V., and Veliev, E. I. (2008). Scattering properties of the strip with fractional boundary conditions and comparison with the impedance strip. *Progress in Electromagnetics Research*, *2*, 189–205.

Alperen, Ö. F., Karaçuha, K., and Tabatadze, V. (2025). Electromagnetic line source scattering by the circular strip with fractional boundary condition. *Journal of Quantitative Spectroscopy and Radiative Transfer*, 109623.

Alperen, Ö. F., Karaçuha, K., and Tabatadze, V. (2023). Electromagnetic scattering of H-polarised cylindrical wave by a double-sided impedance circular strip. *IET Microwaves, Antennas & Propagation*, *17*, 1093–1105.

Biggs, N. R., Chamberlain, P. G., and Moran, C. A. (2016). Embedding formulae for wave diffraction by a circular arc. *Wave Motion*, *67*, 32–46.

CURRICULUM VITAE

Name Surname **:** Ömer Faruk Alperen

EDUCATION **:**

- **B.Sc.** **:** 2016-2017, İstanbul Commerce University, Faculty of Engineering, Department of Electrical and Electronics Engineering
- **M.Sc.** **:** 2019- 2020, İstanbul Technical University, Department of Applied Informatics, Satellite Communication and Remote Sensing

PROFESSIONAL EXPERIENCE AND REWARDS:

- 2018-2020 ISTANBUL Technical University at the Vodafone Future Lab.
- 2020- Researcher Assistant at ISTANBUL Technical University
- 2025- DIPED Conference- In Recognition of the Best Young Scientist Paper Presentation award.

PUBLICATIONS, PRESENTATIONS AND PATENTS ON THE THESIS:

- **Alperen, Ö. F., Karaçuha, K., and Tabatadze, V.** (2025). Electromagnetic line source scattering by the circular strip with fractional boundary condition. *Journal of Quantitative Spectroscopy and Radiative Transfer*, 109623.
- **Alperen, Ö. F., Karaçuha, K., and Tabatadze, V.** (2023). Electromagnetic scattering of H-polarised cylindrical wave by a double-sided impedance circular strip. *IET Microwaves, Antennas & Propagation*, *17*(15), 1093-1105.

OTHER PUBLICATIONS, PRESENTATIONS AND PATENTS:

- **Alperen, Ö. F., Karaçuha, K., Tabatadze, V., & Veliev, E.** (2022). A new approach in electromagnetic plane wave diffraction by two concentric slotted cylinders with variably placed slits: E and H polarized cases. *IET Microwaves, Antennas & Propagation*, *16*(7), 437-450.
- **Alperen, Ö. F., Karaçuha, K., Tabatadze, V., & Veliev, E.** (2022). H-polarized plane wave diffraction by a slotted cylinder with different surface impedances: Solution by the analytical—Numerical approach. *IET Microwaves, Antennas & Propagation*, *16*(14), 869-879.
- **Alperen, Ö. F., Karaçuha, E., Karaçuha, K., Tabatadze, V., & Veliev, E.** (2023). Electromagnetic diffraction by a slotted cylinder with the fractional boundary condition. *Progress in Electromagnetics Research C*, *128*, 61-71.
- **Alperen, Ö. F., Karaçuha, K., Tabatadze, V., & Zaridze, R.** (2022). A New Numerical Approach to Electromagnetic Eigenvalue Problem and Wave Scattering by Conducting Complex-shaped Geometries: Gaussian Basis and Regularized Hankel Functions. *Journal of applied electromagnetism*, *24*(1).
- **Alperen, Ö. F., Joof, S., Karaçuha, K., Tabatadze, V., & Zaridze, R.** (2022). A Simple Approach to Characterize a Buried Object under the Ground. *Prog. Electromagn. Res. M*, *109*, 89-100.